Blade-Wake Interaction Noise for Hovering sUAS Rotors, Part I: Characterization Study

Christopher S. Thurman*
NASA Langley Research Center, Hampton, VA, 23681

James D. Baeder†
University of Maryland, College Park, Maryland, 20742

This work illustrates the use of artificial neural network modeling to study and characterize broadband blade-wake interaction noise from hovering sUAS rotors subject to varying airfoil geometries, rotor geometries, and operating conditions. Design of Experiments was used to create input feature spaces and a high-fidelity strategy was implemented at the discrete data points defined by the input feature spaces to design airfoils and rotor blades, predict the unsteady rotor aerodynamics and aeroacoustics, and isolate the blade-wake interaction noise from the acoustic broadband noise. A metric for the blade-wake interaction noise was developed and the ANOPP2 Artificial Neural Network Tool was used to identify an optimal prediction model for the nonlinear relationship between the input features and the metric for blade-wake interaction noise. This optimal artificial neural network was then validated over training/test data, and exhibited prediction accuracy over 91% for data previously unseen by the model. A sensitivity analysis was conducted, which showed that input features that directly modify the thrust coefficient had a dominant effect over blade-wake interaction noise. The optimal prediction model along with aerodynamic simulations were used to further study the effect of varying input features on blade-wake interaction noise and three types of blade-wake interaction noise were identified.

Nomenclature

a	fluid speed of sound, in/s
C_f	skin friction coefficient
C_T	thrust coefficient
$c(r)$	rotor blade chord length distribution, in
c_{root}	root chord length, in

*Research Aerospace Engineer, Aeroacoustics Branch, 2 N. Dryden St. MS 461, AIAA Member; christopher.thurman@nasa.gov
†Professor, Department of Aerospace Engineering, 3154 Glenn L. Martin Hall, College Park, MD 20742, AIAA Associate Fellow; baeder@umd.edu

c_{tip}	tip chord length, in
e_j	residual between the true value, y_j, and predicted value, $\hat{y}_j$
$f(x_i)$	prediction model output
G_{xx}	power spectral density, Pa^2/Hz
$g(x)$	continuous system representation
k	turbulent kinetic energy, in^2/s^2
L_1	ridge regression regularization
L_2	lasso regression regularization
M_{tip}	Mach number at the rotor blade tip
m	airfoil camber, %chord
N_b	number of rotor blades
n	number of samples in an input feature space
p_{ref}	reference pressure, 20 μPa
R	rotor radius, in
R_d^2	coefficient of determination
Re_{tip}	Reynolds number at the rotor blade tip
r	rotor blade span location normalized by rotor radius
S_i	global sensitivity index corresponding to the i^{th} model input
s	number of input features
T	thrust produced by rotor, lb
TR	taper ratio, $\frac{c_{\text{tip}}}{c_{\text{root}}}$
t/c	airfoil thickness, %chord
U_{fric}	friction velocity, in/s
$\mathbf{u}$	fluid velocity, in/s
v_i	induced rotor velocity, in/s
w	downwash velocity, in/s
$\tilde{\mathbf{x}}$	normalized model input
x_c	nondimensional chord length
$x_i^k, \mathbf{x}_k$	samples in input feature space pertaining to the k^{th} input feature
$\mathbf{y}_j$	j^{th} output from physical system
$\hat{\mathbf{y}}_j$	j^{th} predicted value of $\mathbf{y}_j$
y^+	normalized wall distance

z	neuron output in an artificial neural network
α_0	zero lift angle of attack, deg
γ	activation function used by an artificial neural network neuron
Δf	narrowband spectra frequency resolution, Hz
ΔOB	outer boundary of VR region, in
ϵ	turbulent kinetic energy dissipation rate, in^2/s^3
Θ_{obs}	observer angle relative to rotor plane, deg
$\theta(r)$	rotor twist distribution, deg
θ_{tw}	linear twist, deg
θ_0	collective pitch, deg
μ_p	multiplicative weight between the p^{th} neuron and output layer in an artificial neural network
μ_0	bias term added to the output layer in an artificial neural network
ν	kinematic fluid viscosity, in^2/s
ρ	fluid density, lb/in^3
σ_{mean}	mean rotor solidity
$\sigma(r)$	rotor solidity distribution
τ_{wall}	wall shear stress, lb/in^2
ψ	azimuthal distance between rotor blades, deg
Ω	rotor speed, RPM
ω_{hi}	multiplicative weight between the i^{th} input and h^{th} neuron in an artificial neural network
ω_{h0}	bias term added to the h^{th} neuron in an artificial neural network
ω_i	weight function in the i^{th} direction

I. Introduction

The past decade has seen considerable interest in advanced air mobility (AAM) vehicles, capable of transporting personnel and packages across various environments in a safe and sustainable way. These vehicles are typically comprised of multirotor systems and generally range in size from small unmanned aerial systems (sUAS) (i.e., drones) to single- or multipassenger vehicles designed for operation in urban environments. Though the AAM industry is growing at a rapid pace, noise is still a large inhibitor toward the development and real-world application of these AAM vehicles, which has motivated research in identifying and characterizing noise sources produced by vehicles such as quadcopters, among other types of sUAS vehicles.

The difference in size of these sUAS vehicles, when compared to traditional helicopters, has shown somewhat of a

paradigm shift in the relative importance of different noise-generating mechanisms. For example, it has been shown that the stochastic, or broadband, portion of the noise emanating from such sUAS vehicles lies in the most perceptible range of human audibility and is a dominant noise source when compared to the deterministic, or tonal, noise [1, 2]. This is in contrast to traditional helicopters where tonal noise dominates over broadband and, for this reason, limited work has been done in the prediction and analysis of broadband noise until recently.

There are three types of broadband noise: blade self-noise, turbulence ingestion noise (TIN), and blade-wake interaction (BWI) noise. Blade self-noise, produced by near wake turbulence scattering over a rotor blade trailing edge (i.e., boundary layer dependent), has been studied and modeled extensively [1, 3–10]. TIN noise, caused by the ingestion of atmospheric turbulence into the rotor system, is typically seen in outdoor testing environments [11] and is thought to be prevalent in real-world operation. A low-fidelty TIN prediction model exists [12]; however, due to the random nature of atmospheric turbulence, this noise source is not well understood. BWI noise can be loosely defined as noise caused by blade interactions with rotor-wake turbulence. This rotor-wake turbulence associated with BWI noise is entrained in blade-tip vortices and interacts with subsequent blades in a perpendicular fashion, elucidating the frequently used synonymous term, perpendicular blade-vortex interaction (BVI) noise, in lieu of BWI noise.

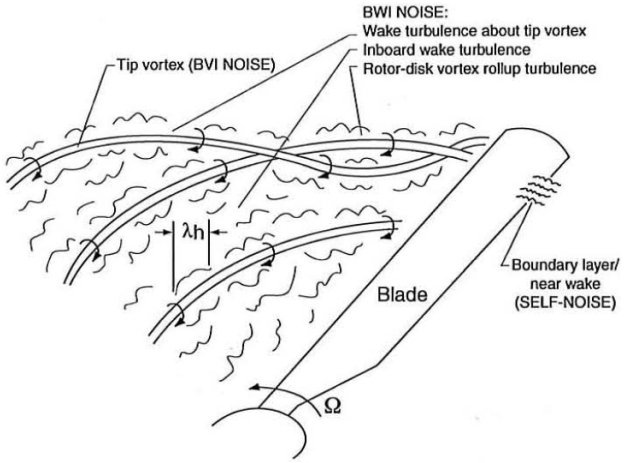

Fig. 1 Illustration of the flowfield encountered by a rotor blade and the associated noise sources. Adapted from Brooks and Burley [13].

BWI noise was first introduced as a prominent broadband noise source by Brooks et al. [14] during a testing campaign over a scaled MBB BO-105 helicopter main rotor performed in the German-Dutch Wind Tunnels (DNW). This work showed that mid-frequency broadband noise was dependent on the rotor tip-path plane (TPP) angle, proving that this mid-frequency noise was related to interactions between rotor blades and shed blade-wake, whereas previously, this noise was believed to be caused by atmospheric turbulence ingestion. Brooks et al. also postulated that, since the TPP angle changes the tip vortex trajectory, this BWI noise is caused by perpendicular BVI events, where the shed blade-wake entrained in the tip vortex interacts with subsequent rotor blades. An example of this can be seen in Fig. 1 taken from Ref. [13]. Since the work in Ref. [14] identified BWI noise by varying the TPP angle, the presence of this noise source was only postulated for forward flight conditions. The introduction of BWI noise promoted further experimental [15–17] and computational [13, 18–20] research to study the characteristics of, and create prediction models for, BWI noise in forward flight conditions.

An analytical model for predicting BWI noise was first developed by Glegg [18], which used the turbulent vortex

model of Phillips and Graham [21] coupled with TIN prediction techniques devised in Refs. [3, 22–24]. This work assumed BWI noise to be caused by turbulence in the tip vortex core, rather than the entrained blade-wake surrounding the tip vortex, and used measured turbulence levels in the vortex core produced by stationary (i.e., nonrotating) airfoils in the prediction scheme. In concluding this work, Glegg hypothesized that BWI noise may be caused by the entrained blade-wake surrounding the tip vortex rather than the assumed turbulence in the vortex core, explaining the poor accuracy of his prediction model. Since it was also established in this work that a more detailed investigation into the tip vortex structure was necessary for accurate predictions, Wittmer et al. [15–17] conducted experimental studies of rectangular NACA 0012 blade planforms downstream of a half-span NACA 0012 used as a vortex generator, shown in Fig. 2. The primary focus of this work was on the tip vortex structure before and after its impingement on the downstream NACA 0012 interaction blade. The findings of this research suggest that there is not enough turbulence surrounding a tip vortex to produce BWI noise until after it has interacted with a downstream blade.

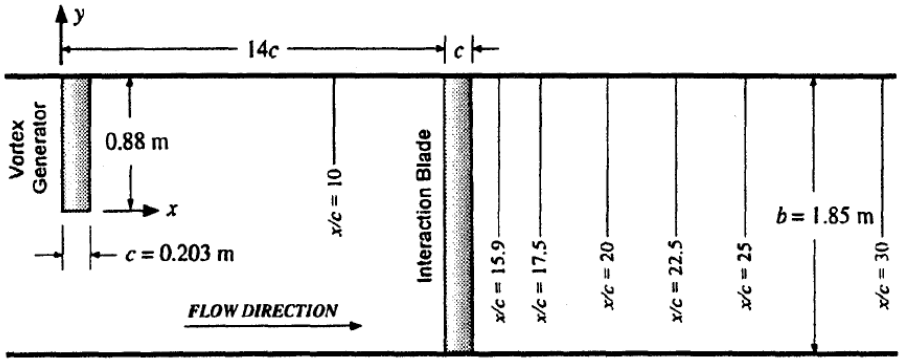

Fig. 2 Illustration of the experimental setup used by Wittmer et al. [16, 17] to study blade-vortex interactions. Adapted with permission from Wittmer and Devenport [16].

The results from Wittmer et al. were used in conjunction with the BWI noise prediction model devised by Glegg [18] in Ref. [19]. A modification to the BWI noise prediction model was implemented where the first BWI event was ignored and only the second and subsequent interactions were considered, which improved the prediction results, though underprediction was still encountered.

Brooks and Burley [13] also devised a BWI prediction methodology, which used cross-spectral relationships between leading edge blade surface pressures and measured acoustic results. Although this prediction method was somewhat accurate, it was highly dependent on the experimental results from the DNW campaign [14] and could not be generalized to other rotors without highly resolved surface pressure data measured at specific leading edge locations on the suction and pressure sides of a rotor blade.

More recently, Thurman et al. [8] showed the presence of BWI noise for a small canonical rotor at various hover operating conditions. High-fidelity lattice-Boltzmann simulations were conducted and the rotor blade surfaces were split into various regions, shown in Fig. 3, to separate acoustic contributions from different regions of the rotor blades at

the observer. It was found that BWI noise from the leading edge region of the blade (i.e., Region IV) was responsible for approximately 6 dB of the total predicted broadband noise, as shown in Fig. 3. It was also shown in Ref. [8] that noise from the rotor without the leading edge region of each blade (i.e., Regions I, II, III, and V) compared well with predictions made using the semiempirical self-noise model of Brooks, Pope, and Marcolini [4]. This finding suggests that BWI noise emanates primarily from the leading edge region (i.e., Region IV) for the rotor geometry used in Ref. [8].

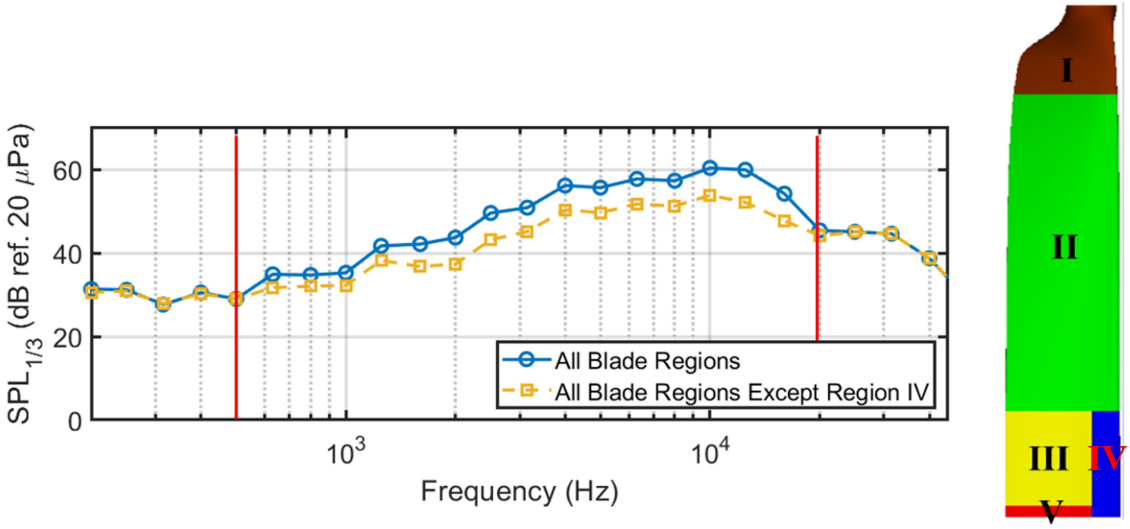

Fig. 3 Acoustic spectra of the calculated broadband noise at an observer located approximately 6.2 ft away from the rotor and $-35°$ below the rotor plane.

Thurman [25] also used the predicted acoustics from the split rotor blade regions shown in Fig. 3 to devise an acoustic metric for BWI noise. This metric was calculated using the difference in overall sound pressure level (OASPL) between the broadband noise from the entire rotor and the rotor without the leading edge region (i.e., Region IV) between 500 Hz and 20 kHz. This BWI noise metric was used with a Design of Experiments (DoE) methodology in an effort to characterize BWI noise under varying collective pitch angles and rotor speeds for the same canonical rotor used in Ref. [8]. This work showed that BWI noise increased with rotor speed, which was believed to be due to increasing tip vortex strength caused by increases in both the induced axial and induced tangential velocities. It was also shown that BWI noise decreased with collective pitch variations about the design operating condition.

The literature review shows that there are substantial deficits in the work done toward understanding and predicting BWI noise. First, BWI noise was only identified as a broadband noise source by varying the TPP angle [14]. The implication of this was that the hover operating condition was assumed to lack BWI noise, which was shown in Refs. [8, 25] to be false. Therefore, no work has been done toward the development of BWI noise prediction models for hovering rotors and very limited work has been done toward acoustic characterization of this broadband noise source at hover operating conditions [25]. Second, the prediction modeling methodology devised by Glegg [18] has only been used with turbulence data from the tip vortex of a fixed, rectangular NACA 0012 blade. It is well known that the loading

distribution of a rotating rotor blade varies significantly from a fixed (i.e., nonrotating) blade [26], meaning that the tip vortex of a rotor blade also differs from that of a fixed blade, elucidating the invalid use of turbulence data from the tip vortices generated by fixed blades. Lastly, all previous work, except that of Refs. [8, 25], has been done for traditional helicopter main rotors with blades consisting of symmetric airfoil profiles. In comparison, sUAS vehicles have largely differing airfoil geometries, rotor geometries, rotor dynamics, and operating conditions; the effects of which have only been sparsely studied.

The objectives of this current work can be summarized as follows:

1) Develop a BWI noise prediction model for hovering sUAS rotors using state-of-the-art machine learning (ML) methodologies. This prediction model will use training data generated from high-fidelity simulations, capable of resolving the turbulence associated with blade-wake entrained in tip vortices. The prediction model will include input parameters commonly associated with sUAS vehicles, such as rotor twist distribution, rotor taper distribution, airfoil camber, airfoil thickness, etc. It should be noted that though rotor blade dihedral and anhedral would serve to modify the tip vortex, the inclusion of such parameters is outside the scope of this work and will be investigated in future BWI noise mitigation studies. The model developed in this work will use a discrete metric for BWI noise, derived in Ref. [25] and in Section II.B.3, to define the BWI noise over a range of frequencies at a single observer location. The prediction model developed herein and the data gathered through this effort will serve as the basis for future prediction modeling efforts to create a BWI noise model capable of predicting acoustic results at any arbitrary observer located in the far field.
2) Utilize the developed BWI noise prediction model for a parameter characterization study. This study will elucidate the effect of varying different input parameters on BWI noise and will indicate which input parameters have the largest influence on BWI noise. This information will further the understanding of BWI noise and will support future broadband noise mitigation studies.

II. Technical Approach

A four-step approach similar to that used in Ref. [10] and shown in Fig. 4 was adopted in this work. Most ML prediction modeling strategies require the apriori development of a sample space consisting of varying combinatorial levels of the input parameters under investigation, which will be discussed in Section II.A. Once the sample space was created, training data were generated at each design point. The generation of these data entailed the use of high-fidelity lattice-Boltzmann simulations and subsequent post-processing techniques discussed in Section II.B. Once the dataset was generated, ML-based approaches, described in Section II.B.4, were used to develop prediction models. These prediction models were then validated and used for the characterization study in Section III.C.

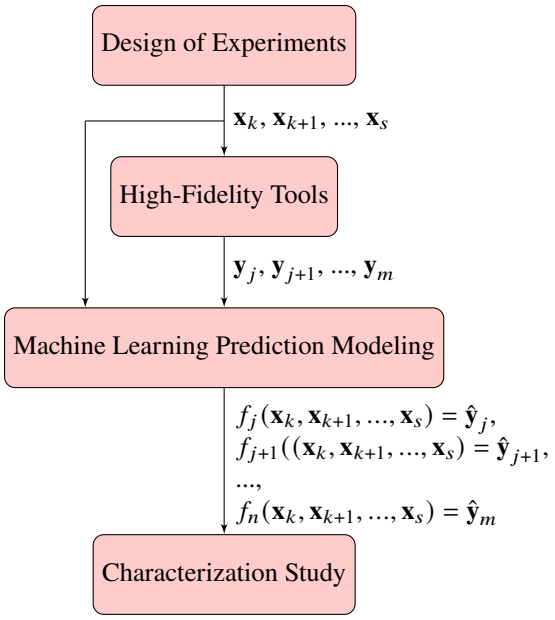

Fig. 4 Block diagram representation of technical approach where $\mathbf{x}_k$ is the k^{th} input feature, $\mathbf{y}_j$ is the j^{th} result using the high-fidelity tools, and f_j is the j^{th} machine learning prediction model used to predict $\hat{\mathbf{y}}_j$.

A. Design of Experiments

DoE is a process used for planning an experiment so that appropriate data can be collected and analyzed by statistical methods, resulting in valid and objective conclusions [27]. DoE is typically used in systems comprised of multiple inputs when a nonlinear functional relationship between the quantities of interest, such as force and moment coefficients, and the regressors, or inputs, and their interactions is required. DoE can be broken up into two categories: classical and modern. A comprehensive study of both categories of DoE was performed by Thurman and Somero [28], which showed the superiority of modern DoE in the context of computer-based experiments. A brief comparison between the two DoE methodologies is given in Table 1.

Table 1 Comparison between classical and modern DoE.

Classical DoE	Modern DoE
Application to physical experiments	Application to computer-based experiments
Fewer experimental points required	More experimental points required
Based upon statistical methodology	No statistical basis; more of an interpolation approach
Fewer available modeling procedures	More available modeling procedures
Factor screening and model reduction	N/A
Limited order of polynomial model (typically $< (xy)^3$)	Unlimited nonlinear modeling capability

Computer-based experiments, such as those performed in this work, are deterministic in nature. This means that

they are only susceptible to systemic error associated with defficiencies related to modeling a physical problem. Typical systemic error arises from grid discretization error, round off error, numerical convergence error, etc., meaning that for a fixed number of iterations, a replicated simulation should produce the same result (i.e., absent of random error). Due to this lack of inherent stochasticism, there is no statistical basis for procedures commonly associated with classical DoE, such as the analysis of variance (ANOVA), which allow for input feature ranking and model reduction. Hence, modern DoE lends itself as a suitable methodology for these deterministic computer-based experiments.

Contrary to classical DoE, which leverages aggressive input feature spacing, modern DoE commonly utilizes a space-filling approach. There are many space-filling designs such as the Latin Hypercube Design (LHD), Sphere-Packing Design, Uniform Design (UD), etc., which all aim to minimize the difference of the overall mean between the physical system being modeled (i.e., continuous), $g(x)$, and the prediction model (i.e., discrete), $f(x_i^k)$, throughout the design space [29]:

$$min\left(\left|\int_{C^N} g(x)dx - \frac{1}{n}\sum_{i=1}^{n} f(x_i^k)\right|\right), \tag{1}$$

where n is the number of samples over the C^N input feature space and k corresponds to each input feature.

In general, space-filling designs can be generated randomly or deterministically. The LHD is the most common example of a randomly generated space-filling design where the elements of each column, k, correspondent to each input feature, are a random permutation of $(1, 2, ..., n)$. Although the LHD is considered to be 'randomly' generated, it outperforms a completely random design space in terms of Eq. 1. To further improve the minimization problem in Eq. 1, various deterministic approaches can be taken that entail an optimization procedure. This optimization typically involves the use of a metric representing the amount of information contained in the distribution of the design space (i.e., entropy [30]) or the uniformity of sample distribution in the design space (i.e., minimax, maximin, etc. [31]). If an optimal design space is created using a uniformity criterion, it is considered to be a UD.

Since ML prediction modeling is an interpolation problem, it is imperative to spread the samples in the design space in a manner which best represents the entirety of the experimental domain. The UD has been shown to successfully achieve this goal in previous studies [10, 28, 32] and was selected as the design space for this work. The creation of this UD followed a threshold-accepting (TA) heuristic [33] over the modified L_2 discrepancy metric [33, 34]. This process was added to the ANOPP2 [35] math module by the main author and a user tool, the ANOPP2 DoE Tool (ADOET), was

developed to allow for quick implementation of the DoE routines via a user namelist. ADOET was modified to allow for the use of one categorical (i.e., discrete) input feature, such as the number of rotor blades, N_b. This modification entailed the design of separate feature spaces at each discrete value of the categorical input feature, with their ensemble yielding the final outputted input feature space. Further details of the UD generation process are provided in Ref. [36].

The input features used in this work were: N_b, rotor radius, R, rotor speed, Ω, linear twist, θ_{tw}, taper ratio, TR, tip chord length, c_{tip}, collective pitch, θ_0, airfoil camber, m, and airfoil thickness, t/c. The location of maximum camber was determined to be both aerodynamically and acoustically insignificant by Thurman et al. [10] and was held constant at 40% chord throughout this work. These input features were chosen due to their potential effect on the blade-wake structure and tip vortex trajectory as well as their tonal and broadband self-noise significance shown in Ref. [10]. The range of the input features was thought to be representative of the entire hover operating condition for typical sUAS rotors. It should be noted that only three- and four-bladed rotors were included in this work due to computational resource limitations and the inclusion of two- and five-bladed rotors in the input feature space is anticipated for future work. The range and type of each input feature are shown in Table 2.

Table 2 Input feature space. (* indicates categorical features. All other features are continuous.)

Input Feature	Range
N_b*	3, 4
R	6 in - 12 in
Ω	3000 RPM - 6000 RPM
θ_{tw}	$-20°$ - $0°$
TR	0.33 - 1
c_{tip}	0.5 in - 1.5 in
θ_0	$-5°$ - $+10°$
m	0% - 10%
t/c	6% - 15%

It is common with ML approaches to split a dataset into training and testing data; however, when using DoE, this data split may produce bias toward specific regions of the design space. For example, if all split training data are located in a particular region of the design space, there will be inadequate coverage over the entirety of the design space to train the prediction model. For this reason, ADOET was used to generate a UD for training data and additional, randomly generated samples were used for test data. Test data are necessary in ML modeling procedures to validate the prediction models against data that were not used in the training procedure. This validation process is vital to ensuring the prediction model can produce accurate predictions everywhere in the design space and can generalize to new data points within the design space that have not previously been seen by the model during the training process.

It was shown by Thurman and Somero [28, 32] that accurate ML prediction models can be generated using eight to

ten samples per input feature in a UD. Since the high-fidelity simulations performed in this work were computationally expensive, the training dataset consisted of 44 samples, or roughly five samples for each of the nine input features, whereas the randomly generated test data had a total of only five samples. Illustrations of the training and test input feature spaces are provided in Fig. 5 where all data points are projected on a 2-D subdimension of the input feature spaces.

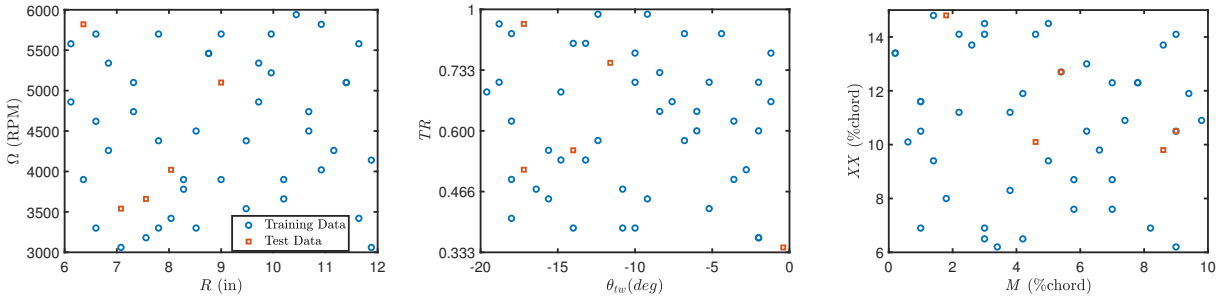

(a) *R* vs. Ω. **(b) θ_{tw} vs. *TR*.** **(c) *m* vs. t/c.**

Fig. 5 Training and test datasets projected on a 2-D input feature space.

B. High-Fidelity Tools

To the authors' knowledge, BWI has yet to be explicitly isolated via experiment. This type of noise emanates from the leading edge of rotor blades, and its isolation from other broadband noise sources (e.g., blade self-noise) can only be accomplished computationally. Because of this, a computational strategy was adopted in this work, which first entailed the design of airfoil geometries and rotor blades. Thurman et al. [8] developed the first computational strategy for the isolation and prediction of BWI noise from a rotor of similar size and operating conditions as the rotors in this work. This BWI noise prediction technique was leveraged in this work and first involved the splitting of the designed rotor blades into various regions. High-fidelity lattice-Boltzmann simulations were then conducted for each rotor design and the acoustic pressure time history (APTH), calculated using the simulated unsteady aerodynamics acting on each rotor blade region, was propagated to a farfield observer location using a time-domain implementation of the Ffowcs Williams and Hawkings acoustic analogy [37]. Different acoustic post-processing techniques were then used to modify the acoustic results before the ML prediction modeling methodology discussed in Section II.B.4 was utilized. The computational approach used throughout this work and its implementation are provided in this Section.

1. Rotor Design

Throughout this work, various computational tools were utilized to allow for rotor designs comprised of the NACA four-digit airfoil geometric parameters: m and t/c, as well as characteristic rotor properties such as N_b, R, Ω, θ_{tw}, TR, c_{tip}, and θ_0. Analytical equations taken from Ladson et al. [38] were used to design the airfoil for each rotor design.

Previous work done by Thurman et al. [10] used an analytical expression to define the twist distribution, $\theta(r)$, which had a functional dependence on the airfoil zero lift angle of attack, α_0, the rotor solidity distribution, $\sigma(r)$, and a target thrust value, $C_{T_{design}}$, calculated apriori:

$$\theta(r) = \frac{1}{r}\left(\frac{4C_{T_{design}}}{5.73\sigma(r)} + \sqrt{\frac{C_{T_{design}}}{2}}\right) - \alpha_0, \tag{2}$$

where r is the normalized span location. Since Eq. 2 is calculated using various rotor properties, the input features from this previous work were highly coupled; with the variation of rotor properties directly affecting $\theta(r)$. In an effort to decouple the inputs for a more direct comparison of their effect on the prediction output, a linear twist distribution, given in Eq. 3, was used in this work:

$$\theta(r) = \theta_0 + \theta_{tw}(r - 0.75), \tag{3}$$

where θ_0 is measured at $0.75R$. To calculate the chord distribution along the span of the blade, $c(r)$, the chord length at the root, c_{root}, was first calculated using Eq. 4:

$$c_{\text{root}} = \frac{c_{\text{tip}}}{TR}. \tag{4}$$

Linear interpolation was then used to determine the chord length distribution, as shown in Eq. 5:

$$c(r) = c_{\text{root}} + r(c_{\text{tip}} - c_{\text{root}}). \tag{5}$$

Typically, sUAS rotors utilize a hub system meaning that the rotor blades must have an inboard root section dedicated to hub installation (e.g., lofted root shank). After defining $\theta(r)$ and $c(r)$ along the entirety of the rotor span, the inboard $0.2R$ was removed from the rotor blades to accommodate any sort of geometry modification necessary for the use of a

hub system. This inboard $0.2R$ was shown to be acoustically insignificant by Thurman et al. [8].

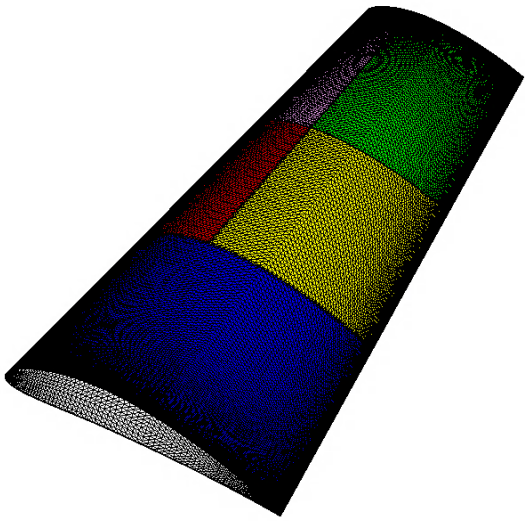

Fig. 6 Orthographic view of tessellated blade surface.

The airfoil coordinates, $\theta(r)$, and $c(r)$ were provided to OpenVSP [39] to generate a CAD representation of the rotor blades that was then tesselated with anisotropic triangular cells using the commercial preprocessing software suite, PowerDELTA 2020-R3, and can be seen in Fig. 6.

Thurman et al. [8] showed that by splitting a rotor blade surface into separate regions, the broadband noise at the observer from each blade region could be ascertained. This methodology allowed for the identification and isolation of BWI noise emanating from the leading edge of each rotor blade. This work used a similar approach to split the rotor blade surface into separate regions, which can be seen in Fig. 7. There are two differences in the splitting approach used in this work when compared to what was done in Ref. [8]. The first is the inclusion of Region III, shown in Fig. 7. Reference [8] showed prominent BWI noise over the outer $0.25R$ of the blade leading edges, however, it was not shown whether BWI noise occurred inboard of this location. The inclusion of Region III in this work will elucidate BWI noise contributions between $0.5R$ and $0.75R$, if any. The second difference between this work and what was done in Ref. [8] is the absence of a region dedicated to the isolation of tip vortex formation noise (Region V in Fig. 3). Tip vortex formation noise is a form of broadband self-noise [4], which is not the primary focus of this study. Because of this, its inclusion in Region IV of Fig. 7 was deemed acceptable.

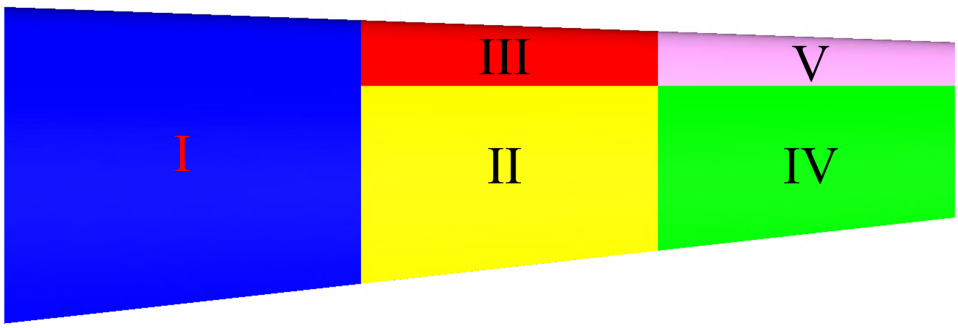

Fig. 7 Top view of split rotor blade surface.

The inboard region, Region I, spanned from $0.2R \leq r \leq 0.5R$ of the blade and included both the suction and pressure side blade surfaces. The second region, Region II, spanned from $0.5R < r \leq 0.75R$ and only included the suction and pressure side blade surfaces from $0.25c < x_c \leq c$. Region III encompassed the leading edge up to the quarter chord location, $0 \leq x_c \leq 0.25c$, of both the suction and pressure sides of the blade between $0.5R < r \leq 0.75R$. Similarly, Regions IV and V spanned the outer $0.25R$ of the blade ($0.75R < r \leq R$) and included the suction and pressure side surfaces from $0.25c < x_c \leq c$ and $0 \leq x_c \leq 0.25c$, respectively. Regions VI and VII, not shown in Fig. 7, correspond to the end caps at the blade root and tip, respectively. Emphasis is drawn away from Regions VI and VII due to their negligible acoustic impact, when compared to Regions I–V. A summary of the spanwise and chordwise extents of Regions I–V is given in Table 3.

Table 3 Split rotor blade region summary.

Region	Spanwise Extents	Chordwise Extents
I	$0.2R < r \leq 0.5R$	$0 \leq x_c \leq c$
II	$0.5R < r \leq 0.75R$	$0.25c < x_c \leq c$
III	$0.5R < r \leq 0.75R$	$0 \leq x_c \leq 0.25c$
IV	$0.75R < r \leq R$	$0.25c < x_c \leq c$
V	$0.75R < r \leq R$	$0 \leq x_c \leq 0.25c$

The final rotors were then assembled within the commercial software suite, PowerCASE 6-2021, using the tesselated blade geometries, where the azimuthal distance between blades was $\psi = \frac{2\pi}{N_b}$. Example rotor geometries are shown in Fig. 8 for clarity.

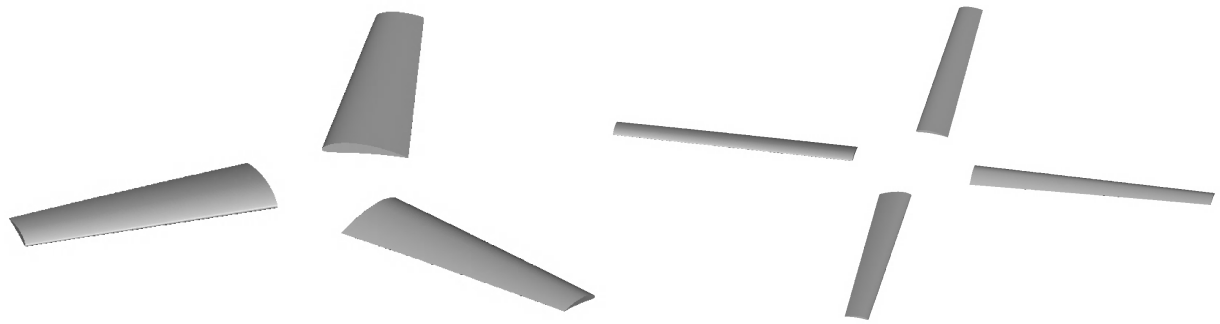

(a) Example of a three-bladed rotor ($N_b = 3$) **(b) Example of a four-bladed rotor ($N_b = 4$).**

Fig. 8 Orthographic view of final rotor geometries.

2. Computational Strategy

The lattice-Boltzmann method (LBM) employed by the commercial software suite, PowerFLOW 6-2021, was used throughout this work due to its proven accuracy on similarly complex rotorcraft problems [2, 8, 40, 41]. LBM is based on kinetic theory and is explicit in nature, solving first for the convection of mesoscopic fluid particles before solving for the collision of these particles on a Cartesian mesh (i.e., lattice). In this work, a statistical description of discrete

particle motion along 19 directions in 3-D space (D3Q19 stencil) was used. The reader is referred to Refs. [42, 43] for a more detailed theoretical explanation of LBM.

Contrary to standard turbulence modeling procedures used by traditional Navier-Stokes solvers, which use closure models to approximate the Reynolds stress as an effective eddy viscosity contribution to the governing equations, PowerFLOW uses a very-large-eddy simulation (VLES) to model the unresolved, subgrid turbulence. The VLES process entails recalibrating the viscous relaxation time in the Boltzmann equation using a turbulent relaxation time calculated via a two-equation $k - \epsilon$ renormalization group (RNG) [44]. Since, in general, LBM involves the use of a Cartesian mesh with isotropic volumetric cells (i.e., voxels), the use of body-fitted, stretched boundary layer grids, like those commonly associated with Navier-Stokes solvers, is not possible. This places a stringent requirement on the number of near-body voxels required to resolve the boundary layer. To circumvent the computational cost associated with this high voxel count, PowerFLOW employs wall-functions in the first voxel adjacent to the geometry to model the boundary layer.

Since PowerFLOW simulations were performed for all samples in the training and test datasets, it was imperative to define an arbitrary computational setup based on rotor properties that could be automated for all training and test data. PowerFLOW automatically discretizes the volumetric computational domain using hexahedron cells (i.e., voxels), provided user-specified variable-resolution (VR) regions. The boundary of two adjacent VR regions contains hanging nodes, where the edge length of the voxels in the coarser region are twice the length of the voxels in the adjacent, finer region, which can be seen in Fig. 9b. Thurman et al. [2, 8] showed that for similar rotor geometries, a cuboidal computational domain extending $10R$ away from the rotor was sufficient for accurate broadband noise prediction. This previous work also showed that a cylindrical VR region dedicated to resolving the rotor wake and extending $2.25R$ away from the center of the rotor was necessary, with a series of seven spherical VR regions growing outward from the wake region to the outer cuboidal boundary of the computational domain, which can be seen in Fig. 9a. This same computational domain was used for all simulations performed in this work.

A grid sensitivity study was performed by Thurman et al. [2], which showed that the finest voxel size in the first VR region adjacent to the rotor should be no larger than approximately $c_{\text{tip}}/250$ for accurate noise predictions from an sUAS rotor with tapered blades. References [8, 25] investigated two different finest voxel sizes, $c_{\text{tip}}/400$ and $c_{\text{tip}}/300$, and it was shown that the coarser of these two resolutions was suitable for BWI noise prediction while substantially reducing the computational cost when compared to the finer resolution. Based on these findings, a finest voxel size of $c_{\text{tip}}/300$

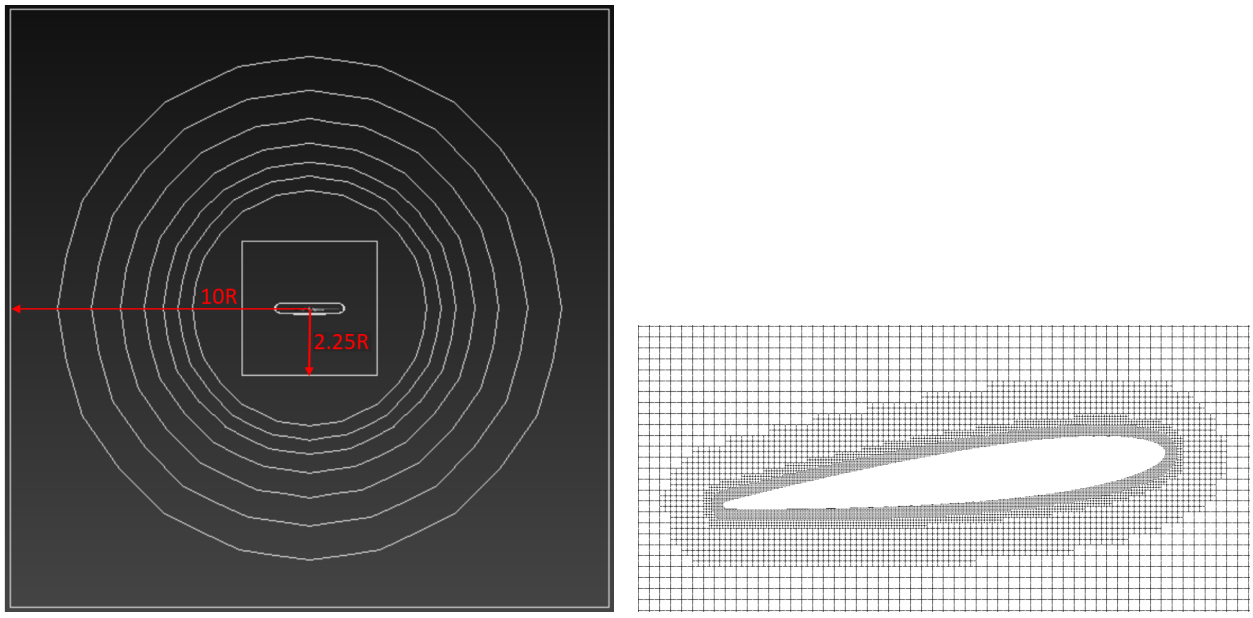

(a) Front view of the volumetric computational domain. **(b) Nearfield resolution regions adjacent to rotor.**

Fig. 9 Illustration of the computational domain used in this work.

was used throughout this work. Similar to this previous work, three VR regions adjacent to the rotor geometry were used. The outer boundary of the first three VR regions, ΔOB, shown in Fig. 9b, was calculated using Eqs. 6 and 7 from White [45], based on y^+ distances of 250, 400, and 1200, respectively:

$$\Delta OB = \frac{y^+ \nu}{U_{fric}}, \tag{6}$$

where

$$U_{fric} = \sqrt{\frac{\tau_{wall}}{\rho}}, \quad \tau_{wall} = \frac{C_f \rho (\Omega R)^2}{2}, \quad C_f = \frac{0.026}{Re_{\text{tip}}}, \quad Re_{\text{tip}} = \frac{(\Omega R) c_{\text{tip}}}{\nu}. \tag{7}$$

A VR region containing the rotor geometry and first three VR regions, shown in Fig. 9a, was also defined with a rotational speed equivalent to the rotor speed and interpolation was used between this rotational VR region and the adjacent stationary computational domain.

A no-slip boundary condition was imposed on the rotor surfaces and ambient standard temperature and pressure (STP) conditions, as well as a zero velocity condition, were imposed on the outer boundaries of the computational

domain for all hover simulations performed in this work. Transitional wall-functions [46**?**] were used to predict the boundary layer behavior on the rotor blade surfaces based on their successful implementation in Ref. [8]. Flowfield convergence was shown to occur near the seventh simulated rotor revolution in Ref. [36], so each simulation was conducted over fourteen rotor revolutions, with the last six being used for acoustic data analysis.

3. Acoustic Post-Processing

Unsteady blade loading was sampled over the last six predicted rotor revolutions at a rate of 133 kHz. These sampled data were then provided to PowerACOUSTICS 6-2021 for the computation of propagated APTH at a defined observer location using a forward-time implementation of Farassat's F1A [47]. Since unsteady loading directly on the blade surfaces was used for this acoustic calculation, it is considered an *impermeable* formulation. PowerACOUSTICS was used was used to propagate the APTH from the impermeable rotor blade surfaces (Regions I – VII in Fig. 7) to an observer located $15R$ away from the center of each rotor and $\Theta_{obs} = -45^{\circ}$ below the rotor plane. This observer location was selected in lieu of others due to broadband noise having a dipole directivity with larger significance out of the rotor plane [36, 48]. It is anticipated that results at other observer locations will be used to develop a BWI noise prediction capability at any arbitrary observer location in a Part II of this work; however, for the proof of concept and characterization purposes of this study, a single observer location was deemed suitable.

The APTH at each observer location calculated using PowerACOUSTICS from the six revolutions of sampled unsteady blade loading was then separated into six equally sized blocks correspondent to each revolution of rotor data. These six revolutions of data were averaged together to obtain a mean revolution of APTH, which is the periodic (i.e., tonal) noise signal. This tonal noise signal was then subtracted from the raw, aperiodic APTH from the six revolutions of data and the resultant residual APTH served as the stochastic (i.e., broadband) noise signal. This technique for periodic averaging and broadband noise signal extraction has been applied extensively to both experimental and computational data with great success in previous work [1, 2, 7–9, 49]. Since broadband noise, and more specifically BWI noise, is the primary focus of this work, only the broadband noise signal was used for further post-processing.

The broadband noise, or residual APTH, was treated as an aperiodic signal over, which a Fast Fourier Transform (FFT) was calculated. The sound pressure level (SPL) of this processed signal was then calculated using Eq. 8 with a frequency resolution, $\Delta f = 50$ Hz, due to the limited number of rotor revolutions of data:

$$\text{SPL} = 10\log_{10}\left(\frac{G_{xx} * \Delta\text{f}}{p_{ref}^2}\right), \tag{8}$$

where G_{xx} is the resultant power spectral density (PSD) from the FFT with units of Pa^2/Hz and $p_{ref} = 20$ μPa. These narrowband broadband noise SPL values were then used to generate one-third octave band ($\text{SPL}_{1/3}$) representations. $\text{SPL}_{1/3}$ values were calculated for the entire rotor, $\text{SPL}_{1/3_{total}}$, as well as for the rotor without the leading edge over the outboard $0.5R$ of the rotor blades (i.e., Regions III and V), $\text{SPL}_{1/3_{total-LE}}$. The difference between these two broadband noise signals was then calculated to obtain the BWI noise represented on a one-third octave band basis:

$$\text{SPL}_{1/3_{BWI}} = \text{SPL}_{1/3_{total}} - \text{SPL}_{1/3_{total-LE}}. \tag{9}$$

It should be noted that $\text{SPL}_{1/3_{BWI}}$ is the relative contribution of BWI noise calculated on a logarithmic basis, which differs drastically from the SPL calculated using the APTH of Regions III and V. The calculated $\text{SPL}_{1/3_{BWI}}$ values were used for preliminary post-processing to distinguish frequencies over which BWI noise was prominent. After initial post-processing of the acoustic results, it was found that some samples in the training and test data had no BWI noise at frequencies below 2500 Hz and above 10 kHz. Because of this, frequencies outside the 2500 Hz to 10 kHz range were omitted from the OASPL calculations performed using Eqs. 10, 11, and 12.

Post-processing methods, similar to what was done in Ref. [25], were used to calculate a discrete BWI noise metric at $\Theta_{obs} = -45°$ to be used for characterization purposes. For this method, the broadband APTH was filtered using a second-order Butterworth bandpass filter between 2500 Hz and 10 kHz. This range restriction ensured that changes in OASPL between samples reflected changes in, and not elimination of, BWI noise. The root mean square value of this resultant filtered signal, $\bar{p}_{rms}$, was used to calculate an OASPL value using the following:

$$\text{OASPL} = 20\log_{10}\left(\frac{\bar{p}_{rms}}{p_{ref}}\right). \tag{10}$$

Equation 10 was used to calculate OASPL values for the entire rotor (OASPL_{total}), the entire rotor without the leading edge over the outboard $0.5R$ of the rotor blades (Regions III and V in Fig. 7), $\text{OASPL}_{total-LE}$, and the entire rotor without the leading edge between the $0.5R$ and $0.75R$ spanwise locations (Region III in Fig. 7), $\text{OASPL}_{total-R3}$. The difference between OASPL_{total} and $\text{OASPL}_{total-R3}$ was calculated via the following:

$$\text{OASPL}_{BWI-R3} = \text{OASPL}_{total} - \text{OASPL}_{total-R3}, \tag{11}$$

which served as the BWI noise metric over Region III to determine this region's contribution to the total BWI noise. The difference between OASPL_{total} and $\text{OASPL}_{total-LE}$:

$$\text{OASPL}_{BWI} = \text{OASPL}_{total} - \text{OASPL}_{total-LE}, \tag{12}$$

was used as the total BWI noise metric, which was calculated for all samples in the training and test input feature spaces and was used as the output quantity for which ML prediction models were trained using techniques discussed in the next Section.

4. Machine Learning Prediction Modeling

In general, ML involves the development of input-output functional relationships, or prediction models, using prescribed input data points ($\mathbf{x}_k, \mathbf{x}_{k+1}, ..., \mathbf{x}_s$; where s corresponds to the number of input features). The ML prediction model is 'trained' over the input data points using some form of algorithmic optimization (e.g., stochastic gradient descent) until the prediction model adequately 'learns' the underlying input-output relationship. The main goal of any ML procedure is not only to fit the input data points, but to develop prediction models that can generalize to new data, previously unseen by the models, to make accuracte predictions anywhere within the prescribed region of experimentation, or input feature space. A detailed discussion on the types of ML tasks and their applicability is provided in Ref. [36]. Artificial neural networks (ANNs) were selected as the ML prediction model architecture used in this work based upon their successful implementation by Thurman and Somero [28, 32] and their proven application to aeroacoustic problems [50, 51]. The ANN aims to replicate the architecture of the neurons in the human brain, set up in layers as shown in Fig. 10. Each "hidden" layer consists of a number of nuerons represented by circles in Fig. 10, aligned in parallel. All neurons of a particular layer are activated in unison, with different multiplicative weights along the connections between neurons, inputs, and outputs. In general, if an ANN has more than one hidden layer, it is considered a multilayer perceptron (MLP); otherwise, it is a single-layer perceptron (SLP).

In the case of the two-layer MLP shown in Fig. 10, the general equations defining the ANN are:

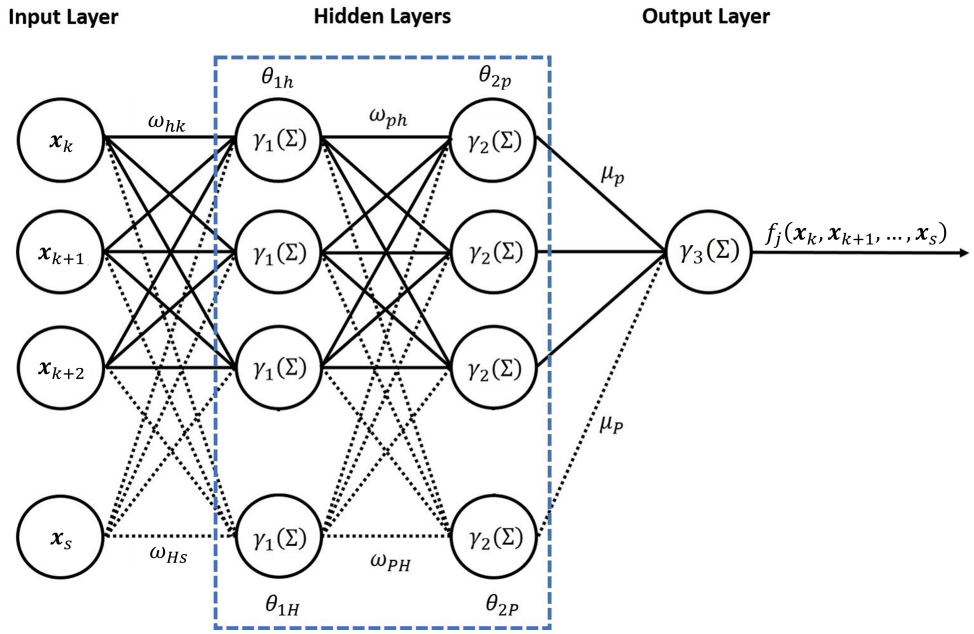

Fig. 10 Illustration of an MLP where the subscripts k, h, and p correspond to the k^{th} input feature, the h^{th} neuron in the first hidden layer, and the p^{th} neuron in the second hidden layer, respectively. The terms ω and μ are multiplicative weights, γ is the activation function evaluated over the summed inputs multiplied by their respective weights, θ are the neurons in a hidden layers, and f_j is the j^{th} ANN prediction model.

$$z_{1h} = \gamma_1\left(\sum_{k=1}^{s} \omega_{hk}\mathbf{x}_k + \omega_{h0}\right), \tag{13}$$

$$z_{2p} = \gamma_2\left(\sum_{h=1}^{H} \omega_{ph}z_{1h} + \omega_{p0}\right), \tag{14}$$

$$f_j(\mathbf{x}_k, \mathbf{x}_{k+1}, \ldots, \mathbf{x}_s) = \gamma_3\left(\sum_{p=1}^{P} \mu_p z_{2p} + \mu_0\right) = \hat{\mathbf{y}}_j, \tag{15}$$

where s is the number of input features, H is the number of neurons in the first hidden layer, and P is the number of neurons in the second hidden layer. In Eq. (13), γ is the activation function used by the neurons in a hidden or output layer, z is the output from a neuron in a hidden layer, ω_{hk} are the weights between the input features and the first hidden layer, ω_{ph} are the weights between the first and second hidden layers, μ_p are the weights between the second hidden layer and the output, ω_0 and μ_0 are commonly used bias terms (i.e., intercepts) added to each hidden layer, and f_j is the j^{th} ANN model producing the predicted values, $\hat{\mathbf{y}}_j$.

The activation functions, γ, can be thought of as functional 'mappings' of a neuron's input onto highly nonlinear

hyperplanes defined by the structure of γ. These activation functions are necessary to introduce nonlinearity to the ANN, enabling it to effectively model complex, nonlinear input-output relationships.

The training procedure for an ANN first involves the random initialization of all weights along the connections between neurons, inputs and outputs. The input data, $(\mathbf{x}_k, \mathbf{x}_{k+1}, ..., \mathbf{x}_s)$, are then provided to the ANN in a feedforward manner and predicted values, $\hat{\mathbf{y}}_j$, are produced. These predicted values are then tested against the provided output, or labeled, data associated with the input data, and a cost function, $\tilde{E}$, is evaluated. This cost function is a numerical description of the error between the labeled output data, $\mathbf{y}_j$, and the predicted output, $\hat{\mathbf{y}}_j$. The error calculated by the cost function is then propagated from the output, $\hat{\mathbf{y}}_i$, back through the ANN via the chain rule of differentiation:

$$\frac{\partial \tilde{E}}{\partial \omega_{hk}} = \frac{\partial \tilde{E}}{\partial \hat{\mathbf{y}}_j} \frac{\partial \hat{\mathbf{y}}_j}{\partial z_{2h}} \frac{\partial z_{2h}}{\partial \omega_{ph}} \frac{\partial \omega_{ph}}{\partial z_{1h}} \frac{\partial z_{1h}}{\partial \omega_{hk}}, \tag{16}$$

where $\partial \tilde{E} / \omega_{hk}$ is the change in error associated with changing the value of the weight, ω_{hk}, between the input layer and the first hidden layer for the two-layer MLP shown in Fig. 10. This method for propagating the error back through the ANN has been coined *backpropagation* by Rumelhart et al. [52]. The gradients calculated using this backpropagation are typically used with an optimization algorithm to update the weights along each connection in the ANN. One optimization cycle through the training data samples, N, is considered to be one *epoch*.

Various forms of regularization are often used in the ANN training process to promote optimization convergence and to help prevent the trained model from overfitting the input data. These regularizations may include normalization of the input data, penalizing $\tilde{E}$ with L_1 (i.e., ridge regression) or L_2 (i.e., lasso regression) regularization, using dropout [53], or randomly eliminating a certain percentage of the neurons in the hidden layer during each epoch of the optimization procedure, and imposing an early stopping criteria on the training process based upon a satisfactory value of $\tilde{E}$. Various ensemble methods such as K-fold cross-validation [54], boosting [55], bootstrap aggregation [56], etc. are also used.

5. Artificial Neural Network Model Development

In general, there are a multitude of different ANN model architectures (number of hidden layers, number of neurons per hidden layer, type of activation function used, etc.), regularization techniques (data scaling, L_1 or L_2 regularization, early stopping, etc.), and hyperparameters that can be used to generate accurate prediction models. These elements of the ANN modeling procedure are typically determined heuristically and are problem specific, varying with the

input-output relationship being modeled. In other words, the optimal ANN structure used for one problem may be different from the ANN structure of another. Because of these potential ANN model form variations as well as the common difficulties associated with creating ANNs, the NASA code, the ANOPP2 Artificial Neural Network Tool (AANNT) [57], was utilized in this work for prediction model development, deployment, and model sensitivity analyses. The reader is referred to Refs. [36] and [57] for more details on the usage and applicability of AANNT.

The prediction model development portion of AANNT was first used to rescale the continuous input features in the input feature space using:

$$\tilde{\mathbf{x}}_k = \frac{\mathbf{x}_k - \mathbf{x}_{k_{min}}}{\mathbf{x}_{k_{max}} - \mathbf{x}_{k_{min}}}, \tag{17}$$

where the subscript, k, corresponds to the number of input features. In Eq. 17, $\tilde{\mathbf{x}}$ corresponds to the rescaled input feature, $\boldsymbol{x}$, ranging from $0 \leq \tilde{\mathbf{x}} \leq 1$. One-hot encoding was used for N_b since it was a categorical input feature. This process of one-hot encoding generates additional binary input features correspondent to the discrete values associated with N_b (i.e., $N_b = 3$ or $N_b = 4$).

Once the data were rescaled, the grid search functionality of AANNT was used to explore various model architectures, which included various combinations of hidden layer activation functions, output layer activation functions, number of neurons in the hidden layers, loss functions used by the optimizer, and various types of regularization (e.g., L_1, L_2, and dropout). The hidden layer activation functions tested in the grid search procedure were the exponential linear unit (ELU), Gaussian error linear unit (GELU) [58], and Swish [59]. ANN architectures including one, two, and three hidden layers consisting of 25, 50, and 100 neurons were also tested in the grid search. Three loss functions were tested in the grid search which included the mean absolute error (MAE), mean squared error (MSE), and HUBER [60], which is a combination of the MAE and MSE loss functions. Various amounts of regularization were tested in the grid search including dropout rates of 0 and 25%, as well as L_1 and L_2 regularization values of 0, 0.01, and 0.1. All models were trained over 2500 epochs using the adaptive moment estimation (ADAM) optimizer [61] and an early stopping criterion was used, which terminated the training procedure if there was no improvement of $\tilde{E}$ after 50 epochs. Training time took approximately 120 seconds per model without early stopping; however, this time was significantly reduced with the early stopping criteria. The total number of trained models in the grid search, based on all possible combinations of the various namelist inputs, was 3888 models. It should be noted that no parallel processing was used for ANN training

throughout this work, however, the training of different models could be performed on different processors, drastically decreasing the overall training time required for the grid search procedure. A table summarizing the different model parameters used in the grid search is provided in 4.

Table 4 Model parameters explored with AANNT grid search.

Hyperparameter	Values
Number of Hidden Layers	1, 2
Number of Neurons in each Hidden Layer	25, 50, 100
Hidden Layer Activation Functions	ELU, GELU, Swish
Output Layer Activation Functions	linear, ELU, GELU, Swish
Loss Functions	MAE, MSE, HUBER
Dropout Rates	0, 25%
L_1 Regularization	0, 0.01, 0.1
L_2 Regularization	0, 0.01, 0.1

The optimal ANN produced by AANNT using these grid search parameters was used over samples in both the training and test data to calculate $\widehat{\text{OASPL}}_{BWI}$ values, where the hat is used to denote a predicted value. These predicted values were then compared against the training/test data values, OASPL_{BWI}, to calculate various error metrics such as the MAE, root mean squared error (RMSE), mean absolute percentage error (MAPE), and the coefficient of determination, R_d^2, which will be discussed in Section III.B.

Lastly, the sensitivity analysis portion of AANNT was used to evaluate the sensitivity of $\widehat{\text{OASPL}}_{BWI}$ to the various input features shown in Table 2 and plots were generated to distinguish trends in $\widehat{\text{OASPL}}_{BWI}$ with the most significant input features. Additionally, flow visualization results were generated to provide further insight to how certain input features affect the tip vortex structure and the BWI event.

III. Results

A. Midspan BWI Significance

In order to distinguish the contribution of Region III in Fig. 7 to the total OASPL_{BWI} noise metric for each sample in the training and test input feature spaces, it was first necessary to calculate OASPL_{BWI-R3}. This metric was then divided by the OASPL_{BWI} value for each sample to calculate its contribution on a relative percentage basis. The OASPL_{BWI-R3} value, as well as its relative percentage of the total OASPL_{BWI}, are shown in Table 5 for samples where the value of OASPL_{BWI-R3} contributed more than 5% of the total OASPL_{BWI}. It should be noted that the full training

and test datasets are available in Ref. [36].

Table 5 Contribution of Region III to the total OASPL_{BWI} for samples where OASPL_{BWI-R3} contributed over 5% of the total.

Sample Number	OASPL_{BWI} (dB)	OASPL_{BWI-R3} (dB)	$100\% * \frac{\text{OASPL}_{BWI-R3}}{\text{OASPL}_{BWI}}$
Training Sample No. 6	1.752115	0.115034	6.57
Training Sample No. 11	4.079201	0.331398	8.12
Training Sample No. 12	4.275085	2.296847	53.73
Training Sample No. 19	5.241988	0.734991	14.02
Training Sample No. 32	6.727732	2.429200	36.12
Training Sample No. 42	5.133381	1.341385	26.13

The samples in Table 5 with OASPL_{BWI-R3} contributions were seen to have negative values of collective pitch, θ_0, and relatively slow rotor speeds, Ω, when compared to the the fastest Ω in the input feature spaces (i.e., Ω = 6000 RPM). It is well known that decreases in Ω will decrease the angles of attack along the blade span, which would be decreased further with negative values of θ_0. Since these rotors aren't trimmed to a target thrust condition, it is likely that the rotors in Table 5 are operating in a turbulent-wake state. To validate this assumption, a vorticity contour generated on a plane aligned with the $c/4$ blade span location of Training Sample No. 12 is shown in Fig. 11. It should be noted that the horizontal lines in all PowerFLOW flowfield visualizations correspond to the interpolation interface between the rotating and stationary VR regions and these VR regions were not exactly aligned.

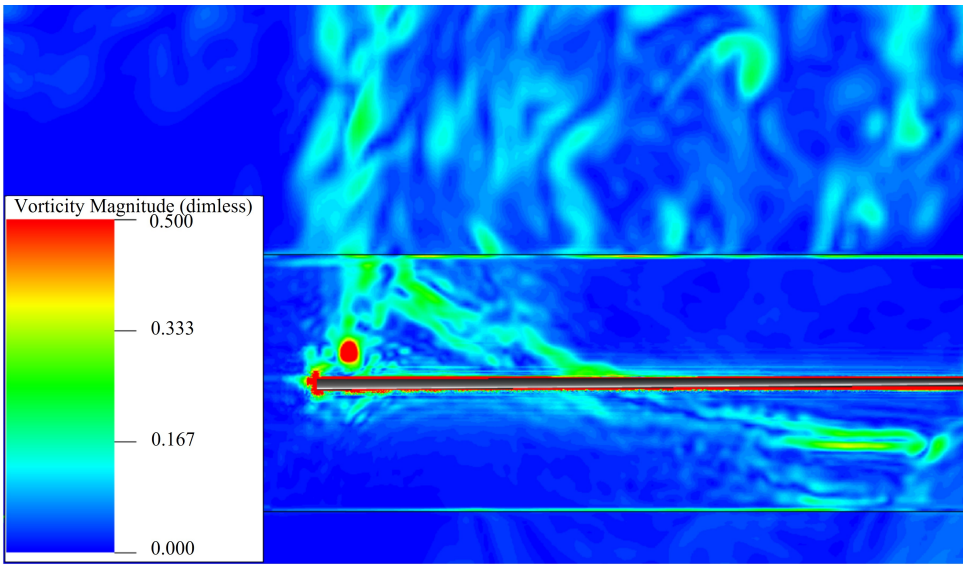

Fig. 11 Vorticity contour of Training Sample No. 12 in Table 5. Turbulent-wake state is shown where vortex convects past suction side of interaction blade.

It can be seen in Fig. 11 that this rotor induces upwash due to the slow rotor speed (Ω = 3300 RPM) and negative value of collective pitch ($\theta_0 = -3.5°$). It can be inferred that this turbulent-wake state is present for all samples in Table 5, which all have significant OASPL_{BWI-R3} contributions caused by the impingement of a blade wake-sheet on subsequent blades, as shown in Fig. 11. Though rotor operation in a turbulent-wake state is undesirable for hover, its inclusion in the input feature spaces elucidates two things:

1) Primary BWI (i.e., caused by impingement of blade-wake entrained in tip vortices) is the dominant source of BWI noise, regardless of whether the tip vortex convects past the suction or pressure side of subsequent blades. This can be ascertained based on the relative contribution of OASPL_{BWI-R3} to OASPL_{BWI} being less than 50% for all but one case in Table 5.
2) Another form of BWI exists in the turbulent-wake state and presumably in mild vertical descent conditions, where BWI noise is generated by the impingement of a blade wake-sheet on the midspan leading edge of a subsequent blade. This secondary form of BWI can cause upward of 2.5 dB of noise for the rotor cases in this work as shown in Table 5.

Since this alternate form of BWI noise only exists for a small subset of samples (operating at undesired flight conditions) in the training and test input feature spaces, its isolation from the total OASPL_{BWI} metric is unneccesary. However, the finding of this alternate BWI noise source may warrant further study.

B. Optimal ANN Prediction Model Validation

Using the grid search procedure in AANNT, an optimal prediction model was identified, which maintained good prediction accuracy over both the training and test data. This ANN had two hidden layers, each consisting of 25 neurons, which used the Swish activation function. The activation function in the output layer was linear, meaning that it served as a summation of the outputs from the second hidden layer, multiplied by the weights of the output layer with the addition of a bias term. All weights and biases associated with the ANN have been tabulated in Appendix C of Ref. [36] for the purpose of replication. It should also be noted that the HUBER loss function was used throughout the training procedure of this ANN, coupled with $L_1 = 0.01$, $L_2 = 0.1$, and no dropout. Though these regularizations are insignificant to the final ANN architecture, they were still used during the training process and should be mentioned.

The optimum ANN was used to make $\widehat{\text{OASPL}}_{BWI}$ predictions over all training and test data samples, along with the calculated residuals, $e_i = \text{OASPL}_{BWI_i} - \widehat{\text{OASPL}}_{BWI_i}$. The predicted values are plotted against the labeled,

output data for both the training and test data in Fig. 12. This figure also includes a dashed line plotted along $\widehat{\text{OASPL}}_{BWI} = \text{OASPL}_{BWI}$ to determine any prediction outliers. As it can be seen, all predicted $\widehat{\text{OASPL}}_{BWI}$ values are relatively close to the actual OASPL_{BWI} values with no significant outliers, indicating good ANN prediction performance over both the training and test data. Another commonly used method for interpreting prediction model results is to plot the residuals, e_i, against the predicted values, $\widehat{\text{OASPL}}_{BWI}$, as shown in Fig. 13.

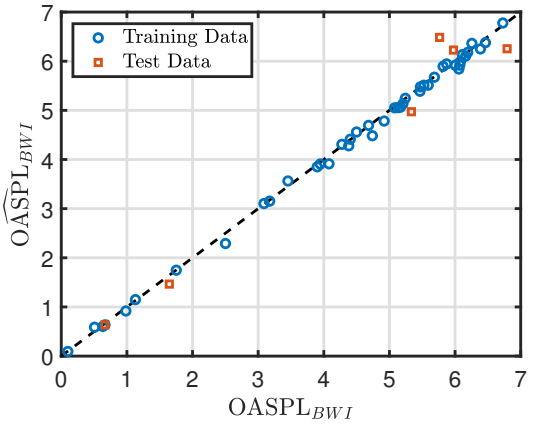

Fig. 12 Predicted $\widehat{\text{OASPL}}_{BWI}$ vs. actual OASPL_{BWI} values

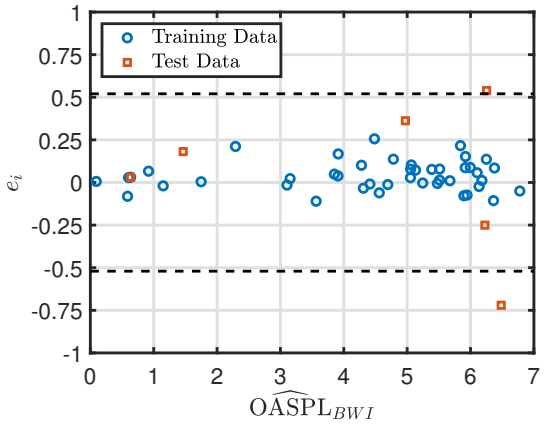

Fig. 13 Residuals, e_j, vs. predicted $\widehat{\text{OASPL}}_{BWI}$ values.

In Fig. 13, the horizontal dashed lines correspond to three standard deviations of the predicted training and test residuals. These results, again, show no significant prediction outliers, further demonstrating the ANNs prediction performance. Other prediction error metrics such as the MAE, MAPE, RMSE, and R_d^2 are shown in Table 6.

Table 6 Optimal ANN prediction error metrics.

	Metrics over training data	Metrics over test data	Metrics over total data
MAE	0.0704	0.4107	0.1051
MAPE	2.28%	8.49%	2.91%
RMSE	0.0927	0.4553	0.1669
R_d^2	0.9975	0.9335	0.9916

In comparing the MAE and RMSE values calculated over the training and test data, respectively, no significant differences are seen. Since the RMSE calculation imposes a larger weight on residual outliers, its negligible difference when compared to the MAE further indicates no significant prediction outliers. In general, the MAE and RMSE values for the training and test data predictions are below the minumum observed OASPL_{BWI} values of 0.1 and 1.646, respectively, elucidating that the ANN is capable of accurate predictions for all samples in both the training and test data.

The MAPE is another commonly used metric for determining prediction modeling performance, with lower percentage values dictating better performance. It can be inferred by the MAPE values in Table 6 that the ANN predictions are 97.72% and 91.51% accurate when compared to the outputted OASPL_{BWI} values. These results indicate that the ANN is not overfit to the training data (i.e., biased) since high prediction accuracy is also observed for the test data, previously unseen by the model. Lastly, the R_d^2 is commonly referred to as a 'goodness of fit' metric, representing the amount of variability in the underlying physical problem accounted for by the prediction model. The high values of 0.9975 and 0.9335 indicate that the ANN accounts for 99.75% and 93.35% of the variability associated with the training and test data, respectively, further illustrating the ANN predictive capabilities over the input feature space. The ANN ability to accurately predict the test data samples, previously unseen by the model, demonstrates that it can generalize well over new data and adequately represents the entirety of the input feature space.

C. BWI Noise Characterization

First-order sensitivity indices, S_k, calculated with the sensitivity analysis portion of AANNT using both Sobol' Sensitivity Analyis [62] and Fourier Amplitude Sensitivity Test (FAST) [63, 64] are shown in descending order, based on input feature ranking, in Table 7. It should be noted that the Sobol' Sensitivity analysis used a Saltelli [65] sample space consisting of 40,960 samples, FAST used a self-named sample space with 36,000 samples, and the optimal ANN was used for predictions at the points in each respective sample space for the sensitivity analyses. In general, model-independent forms of sensitivity analysis can be dependent on the size of the sample space and the predictive precision of the model. Because of this, two sensitivity analysis methods were used, whenever applicable, and the number of points in each respective sample space was increased until sensitivity analysis results were invariant to the size of the sample space, which added robustness to the approach.

Table 7 First-order sensitivity indices.

Feature Ranking	Sobol' Indices	FAST Indices
1	$S_M = 0.1719$	$S_M = 0.1570$
2	$S_\Omega = 0.03592$	$S_\Omega = 0.03701$
3	$S_{c_{\text{tip}}} = 0.03422$	$S_{c_{\text{tip}}} = 0.03539$
4	$S_{t/c} = 0.02799$	$S_{t/c} = 0.03030$
5	$S_{\theta_0} = 0.02521$	$S_{\theta_0} = 0.01693$
6	$S_R = 0.005729$	$S_{TR} = 0.01159$
7	$S_{\theta_{tw}} = 0.005407$	$S_R = 0.008707$
8	$S_{TR} = -0.001950$	$S_{\theta_{tw}} = 0.003015$
9	$S_{N_b} = -0.008320$	$S_{N_b} = 0.001769$

The results from both sensitivity analyses conclude that the amount of airfoil camber, m, has the largest effect on the predicted output, $\widehat{\text{OASPL}}_{BWI}$, followed by Ω, c_{tip}, t/c, and θ_0. It was shown by Zhang et al. [66] that increases in m increase the tip vortex strength while decreasing the amount of shed blade-wake for fixed, rectangular wing sections.

This conclusion suggests that though the tip vortex of a cambered wing may be more capable of entraining blade-wake than a symmetric wing, there is less blade-wake available, implying a reduced turbulent region surrounding the tip vortex. For a rotating wing, increasing m increases the lift generated by a spanwise wing section, thus increasing the thrust, T, generated by the rotor. T is related to the induced velocity, v_i, and downwash speed, w, via the following:

$$v_i = \sqrt{\frac{T}{2\rho\pi R^2}} \quad \text{and} \quad w = 2v_i, \tag{18}$$

meaning that increases in m would not only increase T, but would also increase w, and consequently would increase the vortex miss distance (i.e., vertical separation distance between a tip vortex and the leading edge of a subsequent blade), causing a reduction in BWI noise. This effect can be seen in Fig. 14 where $\widehat{\text{OASPL}}_{BWI}$ was predicted using the ANN model while varying m between its minimum and maximum extents (i.e., 0% and 10%) and keeping all other input features at their mean values (i.e., R = 9 in, Ω = 4500 RPM ($M_{\text{tip}} = 0.32$), $\theta_{tw} = -10°$, $TR = 0.665$, c_{tip} = 1 in ($Re_{\text{tip}} = 193420$), $\theta_0 = 2.5°$, and $t/c = 10.5\%$).

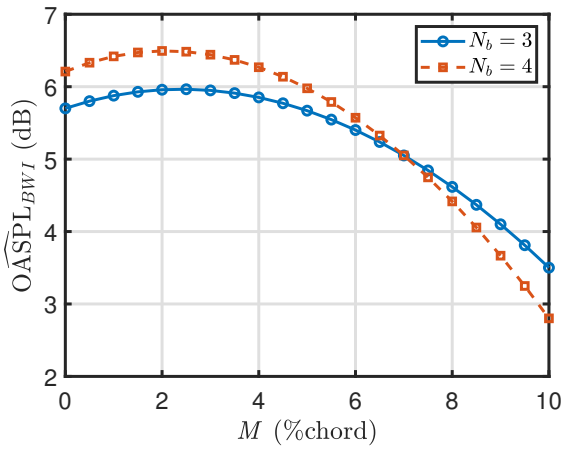

Fig. 14 Effect of varying airfoil camber, m, on $\widehat{\text{OASPL}}_{BWI}$ for 3-bladed and 4-bladed rotors. All other input features were held constant at their mean values of R = 9 in, Ω = 4500 RPM ($M_{\text{tip}} = 0.32$), $\theta_{tw} = -10°$, $TR = 0.665$, c_{tip} = 1 in ($Re_{\text{tip}} = 193420$), $\theta_0 = 2.5°$, and $t/c = 10.5\%$.

Figure 14 also shows that the effect of increasing m is similar for 3-bladed and 4-bladed rotors, however, $\widehat{\text{OASPL}}_{BWI}$ has a larger value for 4-bladed rotors up to $m = 7\%$, which is likely due to the decrease in azimuthal blade spacing (i.e., $\psi = 90°$ vs. $\psi = 120°$) when compared to a 3-bladed rotor. The faster rate of $\widehat{\text{OASPL}}_{BWI}$ decrease for the 4-bladed rotor can be explained by the increased production of T and hence higher w when compared to a 3-bladed rotor with the same input features.

To further illustrate the effect of varying m for 4-bladed rotors, PowerFLOW simulations with a coarse spatial resolution (i.e., $c_{\text{tip}}/200$) were conducted over ten revolutions to visualize the tip vortex and its proximity to the leading edge of subsequent blades for cases with minimum and maximum camber (i.e., $m = 0\%$ and $m = 10\%$), respectively, which are shown in Fig. 15. This figure shows both vorticity and turbulent kinetic energy calculated over an azimuthal slice rotated such that its location is $c_{\text{tip}}/4$ ahead of

the tip of an interactional rotor blade. It should be noted that all other input feature values were held constant at their mean values, similar to what was done in Fig. 14. Calculated T, M_{tip}, and Re_{tip} values have also been provided.

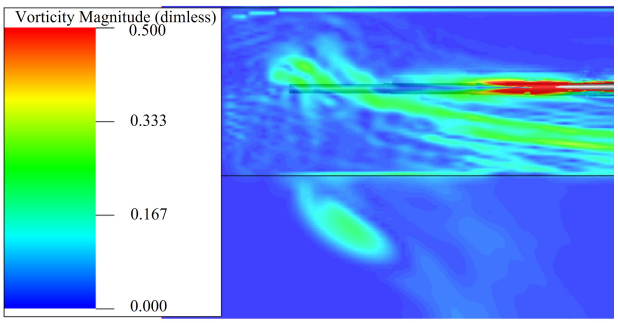

(a) Low camber vorticity: $m = 0\%$**,** $T = 0.53$ **lb,** $M_{\text{tip}} = 0.32$**,** $Re_{\text{tip}} = 193420$**.**

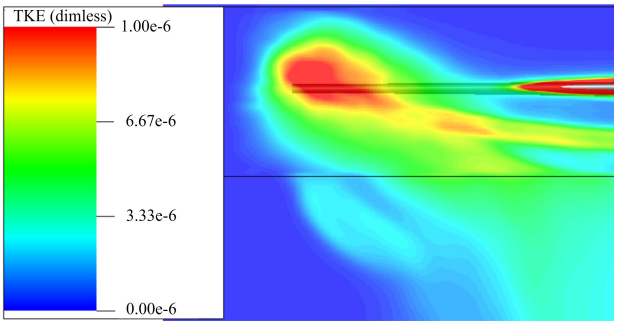

(b) Low camber turbulent kinetic energy: $m = 0\%$**,** $T = 0.53$ **lb,** $M_{\text{tip}} = 0.32$**,** $Re_{\text{tip}} = 193420$**.**

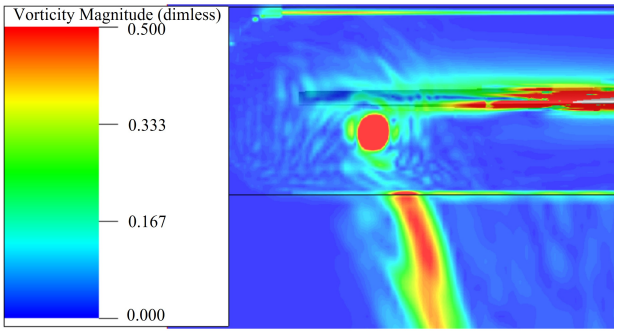

(c) High camber vorticity: $m = 10\%$**,** $T = 6.3$ **lb,** $M_{\text{tip}} = 0.32$**,** $Re_{\text{tip}} = 193420$**.**

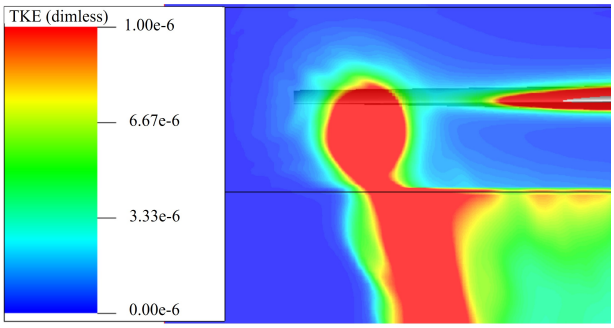

(d) High camber turbulent kinetic energy: $m = 10\%$**,** $T = 6.3$ **lb,** $M_{\text{tip}} = 0.32$**,** $Re_{\text{tip}} = 193420$**.**

Fig. 15 Dimensionless contours illustrating tip vortex impingement for cases with varying airfoil camber, m, for 4-bladed rotors. All other input features were held constant at their mean values of $R = 9$ in, $\Omega = 4500$ RPM, $\theta_{tw} = -10°$, $TR = 0.665$, $c_{\text{tip}} = 1$ in, $\theta_0 = 2.5°$, and $t/c = 10.5\%$.

Figure 15 serves to validate the assumed increase in T and w caused by increasing m. It can be seen that the vortex miss distance does increase with increases in m, however, the leading edge of a subsequent blade is still within the tip vortex region of influence, as shown in Fig. 15d. It is also illustrated in Figs. 15a and 15b that for the 4-bladed case with no camber (i.e., $m = 0\%$), the core of the tip vortex impinges on the leading edge of a subsequent blade, causing vortex bursting, and consequently, higher BWI noise when compared to cambered cases, as seen in Fig. 14. This is an important result because there was initial ambiguity as to whether BWI noise was caused by blade-wake entrained in the tip vortex or by the vortex core itself in the work done by Glegg [18]. All subsequent work [13, 15–17, 19] claimed that BWI noise was due to blade-wake entrained in the tip vortex, however, the findings from Fig. 15 confirm that BWI noise is, in fact, caused by both the blade-wake entrained in the tip vortex and the vortex core itself, with higher BWI noise emission for the latter, in cases with varying m.

Both Ω and c_{tip} serve to modify the Reynolds number at the blade tip, Re_{tip}, and the similar first-order sensitivity index values for these two input features in Table 7 can be accounted for by the linear dependence of Re_{tip} on both of these parameters (i.e., $Re_{\text{tip}} = V_{\text{tip}} c_{\text{tip}} \nu^{-1}$). Though an increase in Re_{tip} would serve to increase the tip vortex strength, it is thought that increasing Ω would also increase the T and w, serving to decrease $\widehat{\text{OASPL}}_{BWI}$. To illustrate this postulation, the effect of varying both Ω and c_{tip} on BWI noise has been plotted in Figs. 16 and 17, respectively. For these two plots, all other input features were held constant at their mean values while Ω and c_{tip} were varied between their minimum and maximum values, respectively, similar to what was done in Fig. 14. To isolate the effect of varying c_{tip} in Fig. 17, TR was held constant at a value of $TR = 1$, representative of a rectangular rotor blade. The value of TR was also held constant at $TR = 1$ for Fig. 16 to provide a more direct comparison between varying Ω and varying c_{tip}. As can be seen in Fig. 16, the $\widehat{\text{OASPL}}_{BWI}$ does indeed decrease with increasing Ω after approximately $\Omega = 4250$ RPM for the 3-bladed case and after approximately $\Omega = 3750$ RPM for the 4-bladed case.

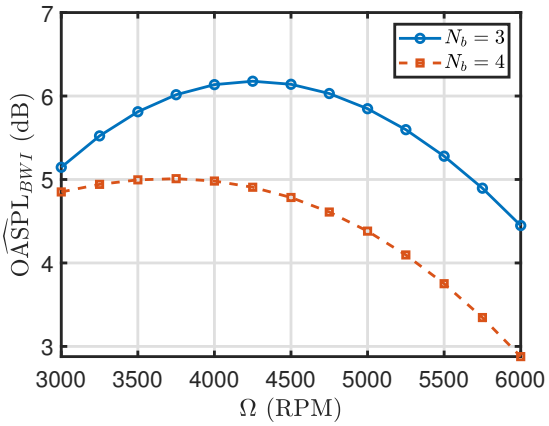

Fig. 16 Effect of varying rotor speed, Ω, on $\widehat{\text{OASPL}}_{BWI}$ for 3-bladed and 4-bladed rotors. All other input features were held constant at their mean values of $R = 9$ in ($0.21 \leq M_{\text{tip}} \leq 0.42$), $\theta_{tw} = -10°$, $c_{\text{tip}} = 1$ in ($128950 \leq Re_{\text{tip}} \leq 257900$), $\theta_0 = 2.5°$, $m = 5\%$, and $t/c = 10.5\%$ except for TR which was set to one.

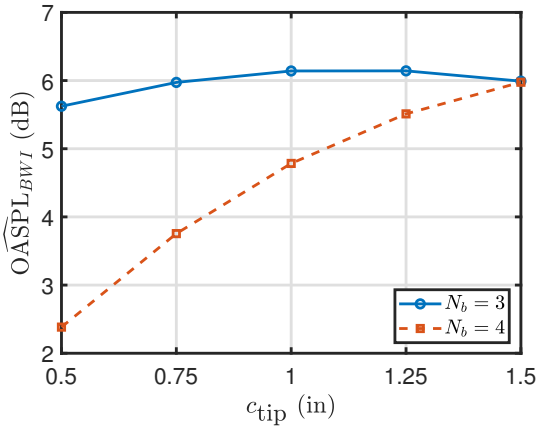

Fig. 17 Effect of varying tip chord length, c_{tip} ($96711 \leq Re_{\text{tip}} \leq 290130$), on $\widehat{\text{OASPL}}_{BWI}$ for 3-bladed and 4-bladed rotors. All other input features were held constant at their mean values of $R = 9$ in, $\Omega = 4500$ RPM ($M_{\text{tip}} = 0.32$), $\theta_{tw} = -10°$, $\theta_0 = 2.5°$, $m = 5\%$, and $t/c = 10.5\%$ except for TR which was set to one.

Coarse resolution PowerFLOW simulations were conducted for cases with varying Ω and c_{tip} in Figs. 18 and 19, respectively, similar to what was done in Fig. 15, however, with a constant value of $TR = 1$. It can be seen from Fig. 18 that although higher values of Ω would increase w, the vortex miss distance does not change when compared to low Ω values. The structure of the tip vortex for the higher Ω case in Fig. 18c does appear to have more entrained

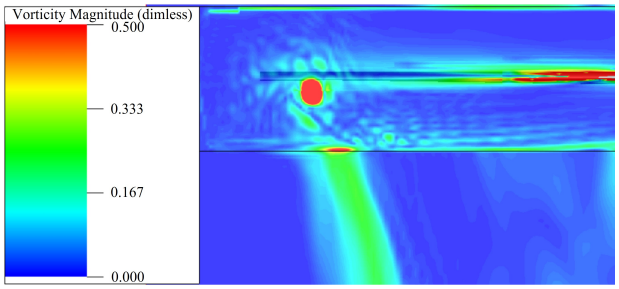

(a) Low rotor speed vorticity: Ω = 3000 RPM, T = 1.3 lb, M_{tip} = 0.21, Re_{tip} = 128950.

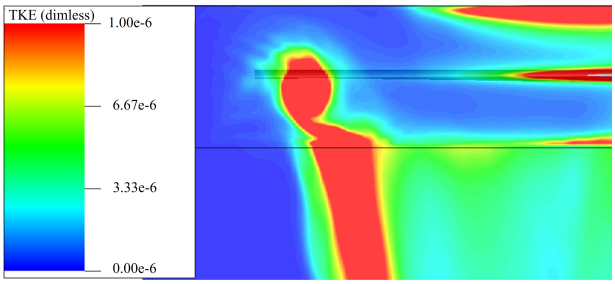

(b) Low rotor speed turbulent kinetic energy: Ω = 3000 RPM, T = 1.3 lb, M_{tip} = 0.21, Re_{tip} = 128950.

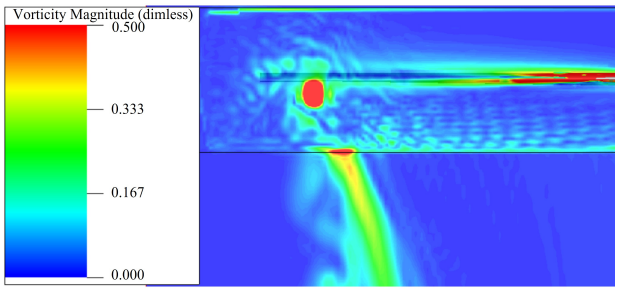

(c) High rotor speed vorticity: Ω = 6000 RPM, T = 5.7 lb, M_{tip} = 0.42, Re_{tip} = 257900.

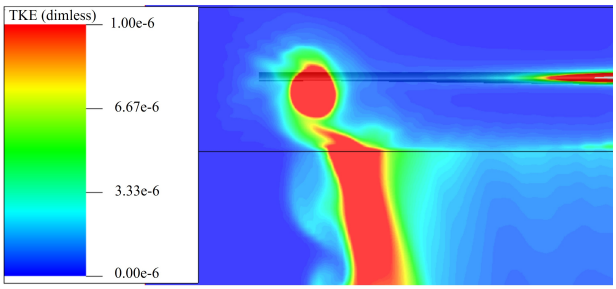

(d) High rotor speed turbulent kinetic energy: Ω = 6000 RPM, T = 5.7 lb, M_{tip} = 0.42, Re_{tip} = 257900.

Fig. 18 Dimensionless contours illustrating tip vortex impingement for cases with varying rotor speed, Ω, for 4-bladed rotors. All other input features were held constant at their mean values of R = 9 in, $\theta_{tw} = -10°$, c_{tip} = 1 in, $\theta_0 = 2.5°$, m = 5%, and t/c = 10.5% except for *TR* which was set to one.

blade-wake and interactional mixing between the tip vortex and blade-wake sheet of preceding blades, possibly caused by the increased Re_{tip}; however, since the tip vortex is stronger for this case, the region of influence is smaller, which can be seen by comparing the turbulent kinetic energy for both rotor speeds in Figs. 18b and 18d, respectively. It is thought that the smaller region of influence for the higher Ω case and hence the increased distance between the center of the vortex core and the leading edge of a subsequent blade may explain the decrease in BWI noise for increases in Ω. This result elucidates that the vortex miss distance is dependent on the thrust coefficient, C_T rather than T, since C_T is typically constant with variations in Ω; however, increases in m would increase both C_T and T, resulting in the previously shown increase in vortex miss distance and resultant decrease in BWI noise.

Increasing c_{tip} would also increase T, though to a lesser extent than for increasing Ω. The results from Fig. 17 indicate that the increased vortex strength due to increases in c_{tip} (i.e., larger Re_{tip}) values serves to increase the BWI noise. This effect is more pronounced for the 4-bladed case when compared to the 3-bladed case.

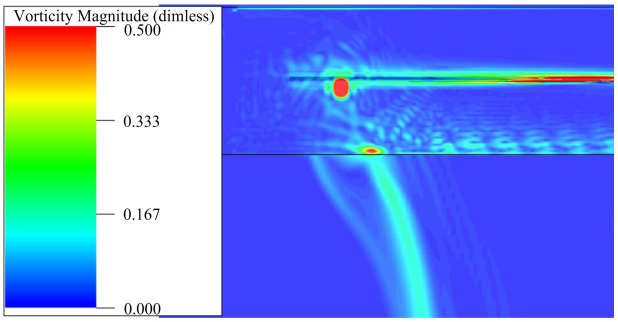

(a) Low tip chord length vorticity: c_{tip} = 0.5 in, T = 2.02 lb, M_{tip} = 0.32, Re_{tip} = 96711.

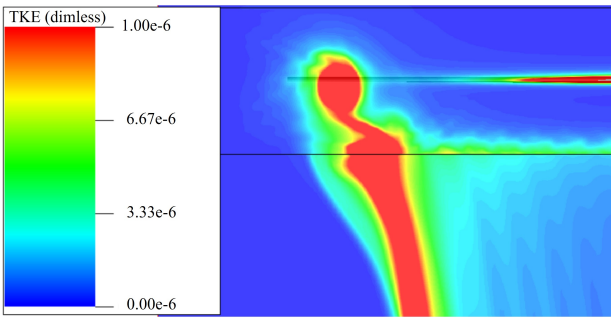

(b) Low tip chord length turbulent kinetic energy: c_{tip} = 0.5 in, T = 2.02 lb, M_{tip} = 0.32, Re_{tip} = 96711.

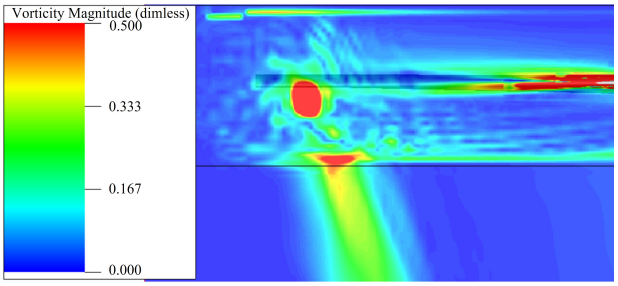

(c) High tip chord length vorticity: c_{tip} = 1.5 in, T = 3.7 lb, M_{tip} = 0.32, Re_{tip} = 290130.

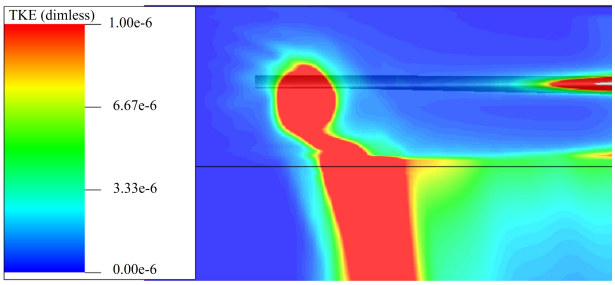

(d) High tip chord length turbulent kinetic energy: c_{tip} = 1.5 in, T = 3.7 lb, M_{tip} = 0.32, Re_{tip} = 290130.

Fig. 19 Dimensionless contours illustrating tip vortex impingement for cases with varying tip chord length, c_{tip}, for 4-bladed rotors. All other input features were held constant at their mean values of R = 9 in, Ω = 4500 RPM, $\theta_{tw} = -10°$, $\theta_0 = 2.5°$, and t/c = 10.5% except for *TR* which was set to one.

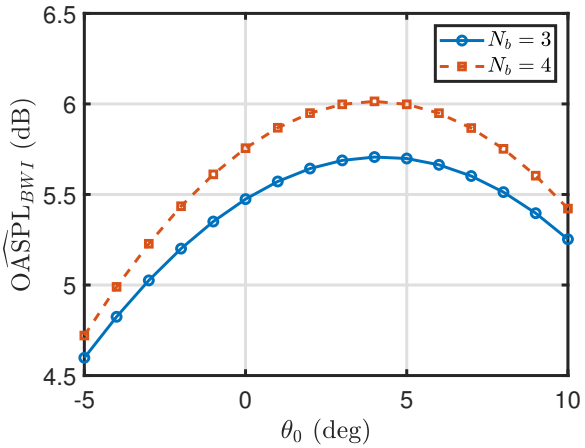

Fig. 20 Effect of varying collective pitch, θ_0, on $\widehat{\text{OASPL}}_{BWI}$ for 3-bladed and 4-bladed rotors. All other input features were held constant at their mean values of R = 9 in, Ω = 4500 RPM (M_{tip} = 0.32), $\theta_{tw} = -10°$, TR = 0.665, c_{tip} = 1 in (Re_{tip} = 193420), m = 5%, and t/c = 10.5%.

PowerFLOW results for cases with both a low c_{tip} (i.e., c_{tip} = 0.5 in) and high c_{tip} (i.e., c_{tip} = 1.5 in), respectively, are shown in Fig. 19. This figure illustrates a more turbulent region surrounding the tip vortex with higher vorticity for the high c_{tip} case in Fig. 19c when compared to the low c_{tip} case in Fig. 19a. This behavior is thought to be caused by the resultant increase in Re_{tip} due to increase in c_{tip}.

It was shown in Section III.A that negative values of collective pitch, θ_0, were seen to cause rotor operation in the turbulent-wake state, causing inboard secondary BWI noise due to a blade wake-sheet impinging on the leading edge of a following blade. It was also shown that the tip

vortex was positioned above the leading edge of subsequent blades in the turbulent-wake state. The effect of increasing θ_0 on the BWI noise has been plotted in Fig. 20 for both a 3-bladed and 4-bladed rotor. It can be ascertained that increasing θ_0 leads to an increase in BWI noise as the tip vortex location changes from above a subsequent blade to below. This implies that there is indeed BWI noise generation while the tip vortex core impinges directly on the leading edge of a blade, contrary to the findings of Wittmer [15–17] for fixed (i.e., nonrotating), symmetric blades. It was shown that increasing a fixed blade section's angle of attack increased the tip vortex strength in Ref. [66] and it is believed that this effect, outside of the turbulent-wake state (i.e., $\theta_0 \geq 0°$), is responsible for the increase in BWI noise. After approximately $\theta_0 = 4°$, Fig. 20 shows a decrease in $\widehat{\text{OASPL}}_{BWI}$, thought to be due to the increased T and w caused by increasing θ_0, similar to what was shown in Fig. 14 for increases in m.

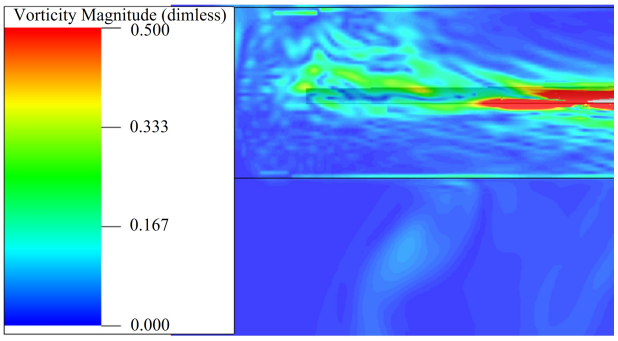

(a) Low collective pitch vorticity: $\theta_0 = -5°$, $T = 0.127$ **lb,** $M_{\text{tip}} = 0.32$, $Re_{\text{tip}} = 193420$.

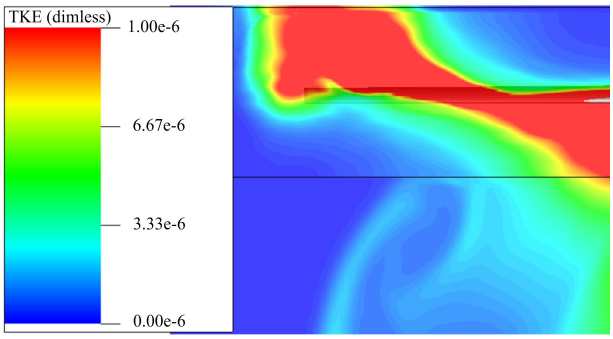

(b) Low collective pitch turbulent kinetic energy: $\theta_0 = -5°$, $T = 0.127$ **lb,** $M_{\text{tip}} = 0.32$, $Re_{\text{tip}} = 193420$.

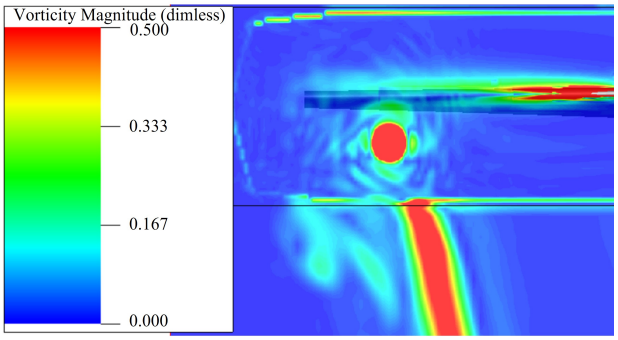

(c) High collective pitch vorticity: $\theta_0 = 10°$, $T = 8.98$ **lb,** $M_{\text{tip}} = 0.32$, $Re_{\text{tip}} = 193420$.

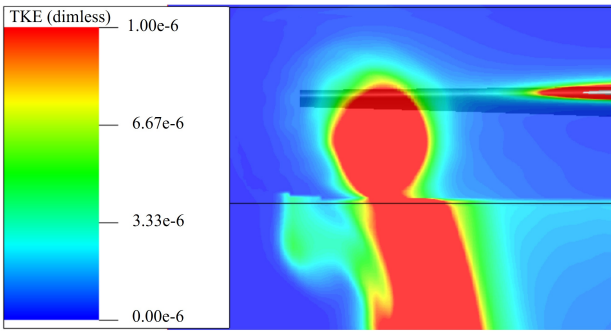

(d) High collective pitch turbulent kinetic energy: $\theta_0 = 10°$, $T = 8.98$ **lb,** $M_{\text{tip}} = 0.32$, $Re_{\text{tip}} = 193420$.

Fig. 21 Dimensionless contours illustrating tip vortex impingement for cases with varying collective pitch, θ_0, for 4-bladed rotors. All other input features were held constant at their mean values of $R = 9$ in, $\Omega = 4500$ RPM, $\theta_{tw} = -10°$, $TR = 0.665$, $c_{\text{tip}} = 1$, $m = 5\%$, and $t/c = 10.5\%$.

PowerFLOW simulations were also conducted for cases with varying θ_0 while keeping all other input features at their mean values, which are shown in Fig. 21. This figure shows similar results to those illustrated in Fig. 15 for

variations in m. It can be seen that for the high θ_0 case (i.e., $\theta_0 = 10°$) in Figs. 21c and 21d, the vortex miss distance is much larger than for variation in other input features. It can be seen that the low θ_0 case in Figs. 21a and 21b exhibits turbulent-wake state rotor operation, with the tip vortex residing some distance above the leading edge of a subsequent blade and with the blade-wake sheet impinging upon the leading edge of a subsequent blade further inboard, causing secondary BWI noise.

It should also be noted that N_b was seen to have a significant effect on $\widehat{\text{OASPL}}_{BWI}$ in all first-order effect plots, however, due to categorical input features having discrete levels, the first-order sensitivity of this input feature was not adequately captured by the sensitivity analyses performed in this work. Coarse resolution PowerFLOW simulations were conducted for 3-bladed and 4-bladed rotor cases while maintaining all other input features at their mean values, which is illustrated in Fig. 22.

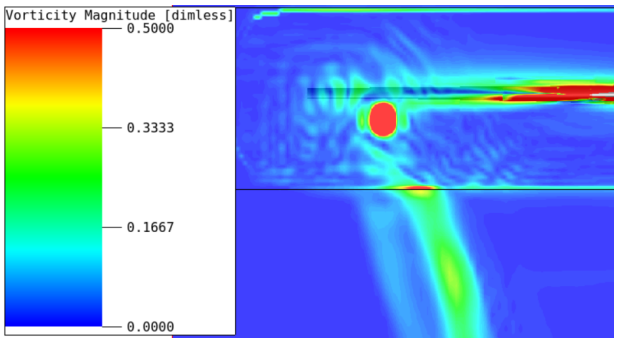

(a) Three-bladed rotor vorticity: $N_b = 3$, $T = 2.87$ **lb,** $M_{\text{tip}} = 0.32$, $Re_{\text{tip}} = 193420$.

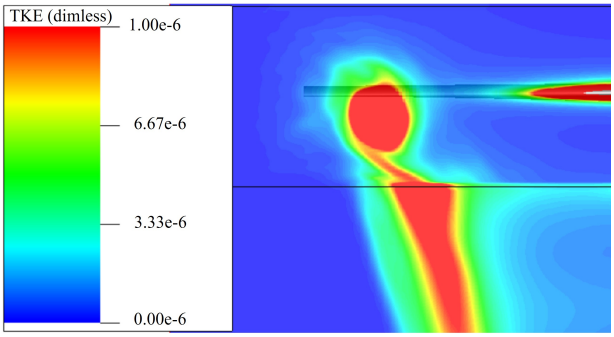

(b) Three-bladed rotor turbulent kinetic energy: $N_b = 3$, $T = 2.87$ **lb,** $M_{\text{tip}} = 0.32$, $Re_{\text{tip}} = 193420$.

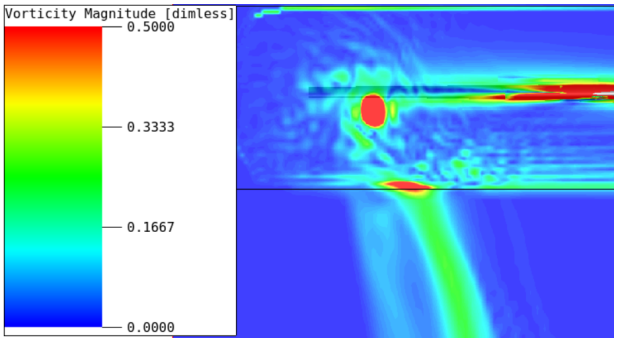

(c) Four-bladed rotor vorticity: $N_b = 4$, $T = 3.26$ **lb,** $M_{\text{tip}} = 0.32$, $Re_{\text{tip}} = 193420$.

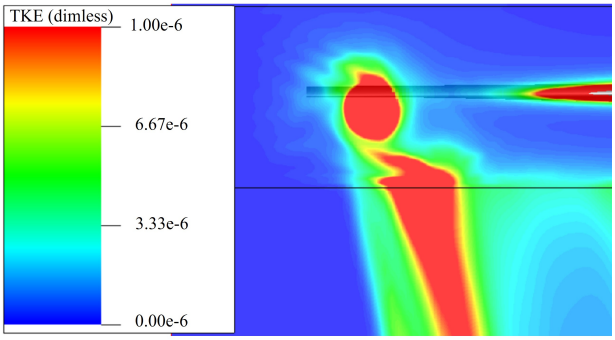

(d) Four-bladed rotor turbulent kinetic energy: $N_b = 4$, $T = 3.26$ **lb,** $M_{\text{tip}} = 0.32$, $Re_{\text{tip}} = 193420$.

Fig. 22 Dimensionless contours illustrating tip vortex impingement for cases with varying number of rotor blades, N_b. All other input features were held constant at their mean values of $R = 9$ in, $\Omega = 4500$ RPM, $\theta_{tw} = -10°$, $TR = 0.665$, $c_{\text{tip}} = 1$ in, $\theta_0 = 2.5°$, $m = 5\%$, and $t/c = 10.5\%$.

It can be seen that although the 4-bladed rotor case generates higher T than the 3-bladed rotor case, the tip vortex has less time to convect downward, which can be seen by comparing the vortex miss distance between the two cases in Fig. 22. Another important result from the 4-bladed rotor case in Fig. 22c is that at the mean $\theta_0 = 2.5°$ value, the tip vortex is below the leading edge of a subsequent blade. When comparing this finding to the resultant effect of varying θ_0, shown in Fig. 20, it can be said that the peak in BWI noise at approximately $\theta_0 = 3.5°$ does not occur during a direct impingement of the tip vortex on the leading edge of a subsequent blade. Rather, maximum BWI noise occurs when the tip vortex is below the leading edge of a subsequent blade, which suggests that there is a specific region in the turbulence field surrounding the tip vortex that is responsible for maximum BWI noise. It is thought that this specific region responsible for maximum BWI noise is that of Region 2 in Fig. 23, or the 'transitional region with eddies of different scales' [67]. Higher order effects are outside the scope of this manuscript; however, the reader is referred to Ref. [36] if interested. It will be noted that second-order effects suggest that the rotor solidity, σ_{mean}, has a large effect on BWI noise.

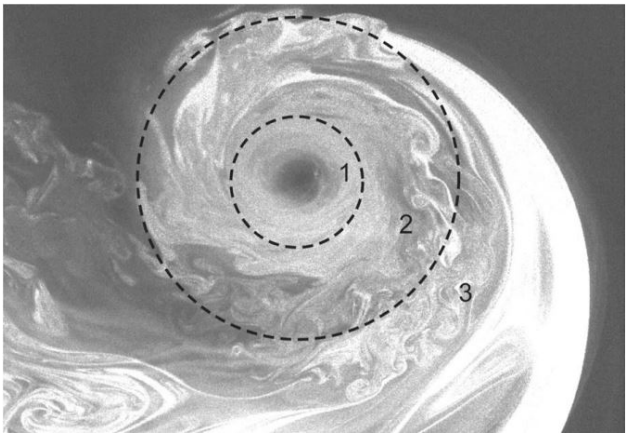

Fig. 23 Laser light sheet flow visualization of a fully developed blade-tip vortex. Adapted with permission from Ramasamy et al. [67].

IV. Conclusions

Prior to this work, only BWI noise for traditional helicopter rotors was studied for forward flight conditions. This previous work assumed BWI noise to be negligible for hovering rotors and efforts toward BWI noise prediction modeling heavily relied on data from fixed, rectangular, symmetric blade sections. This manuscript has not only elucidated the importance of BWI noise for hovering rotors, but also investigated this noise source for sUAS rotors, which has not been done to date. This work also provided a full characterization of BWI noise for hovering sUAS rotors using various input features correspondent to different airfoil and rotor designs, as well as different operating conditions. The results of this work provide fruitful information regarding the cause and types of BWI noise, which can be used for future broadband noise mitigation studies as well as prediction modeling efforts.

It was shown in this work that there are three types of BWI noise for hovering sUAS rotors, where previously, there

was only presumed to be one type. The three types of BWI noise are as follows:

1) The first, and most significant type of BWI noise is the type identified in previous studies, which is caused by impingement of the entrained blade-wake surrounding a tip vortex on the leading edge of a subsequent blade. This primary form of BWI noise is responsible for upward of 7 dB of noise for the rotors in this work.
2) The second-most significant type of BWI noise is caused by a direct impingement of the tip vortex on the leading edge of a subsequent blade. Though this second type of BWI noise may be caused by the bursting of a vortex on the leading edge of a subsequent blade and may not necessarily be influenced by the entrained blade-wake surrounding a tip vortex, the preexisting nomenclature discerning BWI noise (i.e., perpendicular blade-vortex interaction) suggests this form of noise to be BWI noise. Since this type of BWI noise was found by adjusting θ_0, its acoustic magnitude is somewhat arbitrary. However, for the cases in this work involving the variation of θ_0, it can be said that this form of BWI noise can cause approximately 6 dB of noise, which is on par with the acoustic contribution of primary BWI noise.
3) The third and least significant form of BWI noise occurs in turbulent-wake state and mild vertical descent conditions when the blade-wake travels upward through the rotor system. This form of BWI noise is caused by a midspan inpingement of the blade-wake sheet produced by a preceding blade and can cause upward of 2.5 dB of noise.

The characterization study performed in this work showed that the distance between the tip vortex of a preceding blade and the leading edge of a subsequent blade (i.e., vortex miss distance) is not dependent on the thrust produced by a rotor or the correspondent downwash velocity, but is instead dependent on the thrust coefficient. This phenomenon was illustrated by the negligible change in vortex miss distance with varying rotor speeds; however, it was seen that increasing the rotor speed serves to increase the vortex strength, thus reducing the size of its core, which in turn, decreases BWI noise. Input features that directly influence C_T, such as airfoil camber and collective pitch, were seen to have a dominant effect on the vortex miss distance with increases to these input features leading to decreases in BWI noise. BWI noise was shown herein to have the highest sensitivity to airfoil camber, and the work in Ref. [36] showed that this was followed by interactional effects concerning parameters that influence the rotor solidity. Lastly, in comparing the effect of the number of rotor blades and collective pitch on the vortex miss distance, it was seen that direct impingement of a vortex core on the leading edge of a subsequent blade does not cause maximum BWI noise,

rather, there is a specific region in the turbulence field surrounding a tip vortex that is responsible for maximum BWI noise emission.

Though the BWI noise prediction model developed herein provides valuable insight to an important and highly misunderstood broadband noise mechanism, it is limited to the developed input feature space for isolated hovering rotors. Moreover, the prediction model output is only a discrete metric representative of the BWI noise at a single observer location. Subsequent work will use the database and machine learning methodology utilized in this work to develop a full prediction model capable of predicting one-third octave spectra of BWI noise at any arbitrary observer location, which will be the emphasis of a Part II to this work.

V. Acknowledgments

This research is sponsored by the NASA Revolutionary Vertical Lift Technology (RVLT) project. The authors would like to thank the National Institute of Aerospace (NIA), the NIA Langley Professor Program, and Mary Catherine Bunde of the NIA for the kindness, support, and facilitation through this academic journey and for making this work possible. Computational resources necessary for this work were provided by both the NASA High-End Computing (HEC) Program through the NASA Advanced Supercomputing (NAS) Division at the Ames Research Center and the Midrange HPC K-Cluster at the Langley Research Center.

References

[1] Zawodny, N. S., Boyd Jr., D. D., and Burley, C. L., "Acoustic Characterization and Prediction of Representative, Small-Scale Rotary-Wing Unmanned Aircraft System Components," *AHS International 72nd Annual Forum & Technology Display, West Palm Beach, FL*, May 2016.

[2] Thurman, C. S., Zawodny, N. S., and Baeder, J. D., "Computational Prediction of Broadband Noise from a Representative Small Unmanned Aerial System Rotor," *VFS International 76th Annual Forum & Technology Display, Virtual*, October 2020. https://doi.org/10.4050/F-0076-2020-16492.

[3] Amiet, R. K., "Acoustic Radiation from an Airfoil in a Turbulent Stream," *Journal of Sound and Vibration*, Vol. 41, No. 4, 1975, pp. 407–420. https://doi.org/10.1016/S0022-460X(75)80105-2.

[4] Brooks, T. F., Pope, D. S., and Marcolini, M. A., "Airfoil Self-Noise and Prediction," NASA RP 1218, 1989.

[5] Li, S., and Lee, S., "UCD-QuietFly: A New Program to Predict Multi-Rotor eVTOL Broadband Noise," *2020 VFS Aeromechanics for Advanced Vertical Flight Technical Meeting, San Jose, CA*, 2020.

[6] Burley, C. L., and Brooks, T. F., "Rotor Broadband Noise Prediction with Comparison to Model Data," *Journal of the American Helicopter Society*, Vol. 49, No. 1, 2004, pp. 28–42. https://doi.org/10.4050/JAHS.49.28.

[7] Pettingill, N. A., and Zawodny, N. S., "Identification and Prediction of Broadband Noise for a Small Quadcopter," *VFS International 75th Annual Forum & Technology Display, Philadelphia, PA*, May 2019.

[8] Thurman, C. S., Zawodny, N. S., Pettingill, N. A., Lopes, L. V., and Baeder, J. D., "Physics-informed Broadband Noise Source Identification and Prediction of an Ideally Twisted Rotor," *AIAA SciTech 2021 Forum, Virtual*, AIAA Paper 2021–1925, January 2021. https://doi.org/10.2514/6.2021-1925.

[9] Pettingill, N. A., Zawodny, N. S., Thurman, C. S., and Lopes, L. V., "Acoustic and Performance Characteristics of an Ideally Twisted Rotor in Hover," *AIAA SciTech 2021 Forum, Virtual*, AIAA Paper 2021–1928, January 2021. https://doi.org/10.2514/6.2021-1928.

[10] Thurman, C. S., and Zawodny, N. S., "Aeroacoustic Characterization of Optimum Hovering Rotors using Artificial Neural Networks," *VFS International 77th Annual Forum & Technology Display, Virtual*, May 2021. https://doi.org/10.4050/F-0077-2021-16683.

[11] Fleming, J., Langford, M., Gold, J., Schwartz, K., Wisda, D., Alexander, N., and Whelchel, J., "Measured Acoustic Characteristics of Low Tip Speed eVTOL Rotors in Hover," *VFS International 78th Annual Forum & Technology Display, Fort Worth, TX*, May 2022. https://doi.org/10.4050/F-0078-2022-17434.

[12] Amiet, R. K., "Noise Produced by Turbulent Flow Into a Rotor: Theory Manual for Noise Calculation," NASA CR 181788, 1989.

[13] Brooks, T. F., and Burley, C. L., "Blade Wake Interaction Noise for a Main Rotor," *Journal of the American Helicopter Society*, Vol. 49, No. 1, 2004, pp. 11–27. https://doi.org/10.4050/JAHS.49.11.

[14] Brooks, T. F., Marcolini, M. A., and Pope, D. S., "Main Rotor Broadband Noise Study in the DNW," *Journal of the American Helicopter Society*, Vol. 34, No. 2, 1989, pp. 3–12. https://doi.org/10.4050/JAHS.34.2.3.

[15] Wittmer, K. S., Devenport, W. J., Rife, M. C., and Glegg, S. A. L., "Perpendicular Blade Vortex Interaction," *AIAA Journal*, Vol. 33, No. 9, 1995, pp. 1667–1674. https://doi.org/10.2514/3.12802.

[16] Wittmer, K. S., and Devenport, W. J., "Effects of Perpendicular Blade-Vortex Interaction, Part 1: Turbulence Structure and Development," *AIAA Journal*, Vol. 37, No. 7, 1999, pp. 805–812. https://doi.org/10.2514/2.7527.

[17] Wittmer, K. S., Devenport, W. J., and Glegg, S. A. L., "Effects of Perpendicular Blade-Vortex Interaction, Part 2: Parameter Study," *AIAA Journal*, Vol. 37, No. 7, 1999, pp. 813–817. https://doi.org/10.2514/2.7528.

[18] Glegg, S. A. L., "Prediction of Blade Wake Interaction Noise Based on a Turbulent Vortex Model," *AIAA Journal*, Vol. 29, No. 10, 1991, pp. 1545–1551. https://doi.org/10.2514/3.10774.

[19] Glegg, S. A. L., Devenport, W. J., Wittmer, K. S., and Pope, D. S., "Broadband Helicopter Noise Generated by Blade Wake Interactions," *Journal of the American Helicopter Society*, Vol. 44, No. 4, 1999, pp. 293–301. https://doi.org/10.4050/JAHS.44.293.

[20] Mauffrey, Y., Rahier, G., and Prieur, J., "Numerical Investigation on Blade/Wake-Interaction Noise Generation," *Journal of Aircraft*, Vol. 46, No. 5, 2009, pp. 1479–1486. https://doi.org/10.2514/1.32390.

[21] Phillips, W. R. C., and Graham, J. A. H., "Reynolds-Stress Measurements in a Turbulent Trailing Vortex," *Journal of Fluid Mechanics*, Vol. 147, 1984, pp. 353–371. https://doi.org/10.1017/S0022112084002123.

[22] Paterson, R. W., and Amiet, R. K., "Noise of a Model Helicopter Rotor Due to Ingestion of Turbulence," NASA CR 3213, 1979.

[23] Glegg, S. A. L., "Significance of Unsteady Thickness Noise Sources," *AIAA Journal*, Vol. 25, No. 6, 1987, pp. 839–844. https://doi.org/10.2514/3.9709.

[24] Glegg, S. A. L., Baxter, S. M., and Glendinning, A. G., "The Prediction of Broadband Noise from Wind Turbines," *Journal of Sound and Vibration*, Vol. 118, No. 2, 1987, pp. 217–239. https://doi.org/10.1016/0022-460X(87)90522-0.

[25] Thurman, C. S., "Characterization of Blade Wake Interaction Noise for an Ideally Twisted Rotor," *NASA Acoustics Technical Working Group Meeting, Virtual*, April 2021.

[26] Komerath, N., Ganesh, B., and Wong, O., "On the Formation and Decay of Rotor Blade Tip Vortices," *34th AIAA Fluid Dynamics Conference and Exhibit, Portland, OR*, AIAA Paper 2004-2431, June 2004. https://doi.org/10.2514/6.2004-2431.

[27] Montgomery, D. C., *Design and Analysis of Experiments*, John Wiley & Sons, New York, NY, 1984.

[28] Thurman, C. S., and Somero, J. R., "Comparison of Meta-Modeling Methodologies through the Statistical-Empirical Prediction Modeling of Hydrodynamic Bodies," *Journal of Ocean Engineering*, Vol. 210, No. 107566, 2020. https://doi.org/10.1016/j.oceaneng.2020.107566.

[29] Fang, K.-T., Li, R., and Sudjianto, A., *Design and Modeling for Computer Experiments*, Chapman and Hall/CRC, New York, NY, 2005.

[30] Shannon, C. E., "A Mathematical Theory of Communication," *The Bell System Technical Journal*, Vol. 27, No. 3, 1948, pp. 379–423.

[31] Johnson, M. E., Moore, L. M., and Ylvisaker, D., "Minimax and Maximin Distance Designs," *Journal of Statistical Planning and Inference*, Vol. 26, No. 2, 1990, pp. 131–148. https://doi.org/10.1016/0378-3758(90)90122-B.

[32] Thurman, C. S., and Somero, J. R., "Hydrodynamic Characterization of Bodies of Revolution through Statistical-empirical Prediction Modeling using Machine Learning," *Journal of Ship Research*, Vol. 66, June 2022, pp. 182–191. https://doi.org/10.5957/JOSR.06200035.

[33] Fang, K.-T., Lin, D., Winker, P., and Zhang, Y., "Uniform Design: Theory and Application," *Technometrics*, Vol. 42, No. 3, 2000, pp. 237–248. https://doi.org/10.2307/1271079.

[34] Hickernell, F. J., "A Generalized Discrepancy and Quadrature Error Bound," *Mathematics of Computation*, Vol. 67, No. 221, 1998, pp. 299–322. https://doi.org/10.1090/S0025-5718-98-00894-1.

[35] Lopes, L. V., and Burley, C. L., "ANOPP2 User's Manual: Version 1.2," NASA TM 2016-219342, 2016.

[36] Thurman, C. S., "Surrogate Modeling and Characterization of Blade-Wake Interaction Noise for Hovering sUAS Rotors using Artificial Neural Networks," Ph.D. thesis, University of Maryland, College Park, MD, July 2022.

[37] Ffowcs Williams, J. E., and Hawkings, D. L., "Sound Generation by Turbulence and Surfaces in Arbitrary Motion," *Philosophical Transactions of the Royal Society of London. Series A, Mathematical and Physical Sciences*, Vol. 264, No. 1151, 1969, pp. 321–342. https://doi.org/10.1098/rsta.1969.0031.

[38] Ladson, C. L., Brooks Jr., C. W., Hill, A. S., and Sproles, D. W., "Computer Program to Obtain Ordinates for NACA Airfoils," NASA TM 4741, 1996.

[39] McDonald, R. A., and Gloudemans, L. R., "Open Vehicle Sketch Pad: An Open Source Parametric Geometry and Analysis Tool for Conceptual Aircraft Design," *AIAA Scitech 2022 Forum, San Diego, CA & Virtual*, AIAA Paper 2022-0004, January 2022. https://doi.org/10.2514/6.2022-0004.

[40] Nardari, C., Casalino, D., Polidoro, F., Coralic, V., Brodie, J., and Lew, P., "Numerical and Experimental Investigation of Flow Confinement Effects on UAV Rotor Noise," *25th AIAA/CEAS Aeroacoustics Conference, Delft, The Netherlands*, AIAA Paper 2019–2497, May 2019. https://doi.org/10.2514/6.2019-2497.

[41] Casalino, D., Grande, E., Romani, G., Ragni, D., and Avallone, F., "Definition of a Benchmark for Low Reynolds Number Propeller Aeroacoustics," *Aerospace Science and Technology*, Vol. 113, No. 106707, 2021. https://doi.org/10.1016/j.ast.2021.106707.

[42] Succi, S., *The Lattice Boltzmann Equation for Fluid Dynamics and Beyond*, 1st ed., Clarendon Press, Oxford, 2001.

[43] Shan, X., Yuan, X.-F., and Chen, H., "Kinetic Theory Representation of Hydrodynamics: a Way Beyond the Navier-Stokes Equation," *Journal of Fluid Mechanics*, Vol. 550, 2006, pp. 413–441. https://doi.org/10.1017/S0022112005008153.

[44] Yakhot, V., and Orszag, S. A., "Renormalization Group Analysis of Turbulence. I. Basic Theory," *Journal of Scientific Computing*, Vol. 1, No. 1, 1986, pp. 3–51. https://doi.org/10.1007/BF01061452.

[45] White, F. M., *Fluid Mechanics*, WCB/McGraw-Hill, Boston, MA, 1999.

[46] Exa Corporation, Burlington, MA (US), "Computer Simulation of Physical Processes Including Modeling of Laminar-to-Turbulent Transition," *US 2014/0136159 A1*, 2014.

[47] Casalino, D., "An Advanced Time Approach for Acoustic Analogy Predictions," *Journal of Sound and Vibration*, Vol. 261, No. 4, 2003, pp. 583–612. https://doi.org/10.1016/S0022-460X(02)00986-0.

[48] Brentner, K., and Farassat, F., "Modeling aerodynamically generated sound of helicopter rotors," *Progress in Aerospace Sciences*, Vol. 39, No. 2–3, 2003, pp. 83–120. https://doi.org/10.1016/S0376-0421(02)00068-4.

[49] Thurman, C. S., Zawodny, N. S., and Pettingill, N. A., "The Effect of Boundary Layer Character on Stochastic Rotor Blade Vortex Shedding Noise," *VFS International 78th Annual Forum & Technology Display, Fort Worth, TX*, May 2022. https://doi.org/10.4050/F-0078-2022-17428.

[50] Greenwood, E., "Estimating Helicopter Noise Abatement Information with Machine Learning," *AHS International 74th Annual Forum & Technology Display, Phoenix, AZ*, May 2018.

[51] Li, S., and Lee, S., "A Machine Learning-Based Fast Prediction of Rotorcraft Broadband Noise," *AIAA AVIATION 2020 Forum, Virtual*, AIAA Paper 2020-2588, June 2020. https://doi.org/10.2514/6.2020-2588.

[52] Rumelhart, D. E., Hinton, G. E., and Williams, R. J., "Learning Representations by Back-propagating Errors," *Nature*, Vol. 323, 1986, pp. 533–536. https://doi.org/10.1038/323533a0.

[53] Srivastava, N., Hinton, G., Krizhevsky, A., Sutskever, I., and Salakhutdinov, R., "Dropout: A Simple Way to Prevent Neural Networks from Overfitting," *Journal of Machine Learning Research*, Vol. 15, No. 56, 2014, pp. 1929–1958.

[54] Bouckaert, R. R., "Choosing between Two Learning Algorithms based on Calibrated Tests," *20th International Conference on Machine Learning, Washington, D.C.*, August 2003.

[55] Schapire, R. E., "The Strength of Weak Learnability," *Machine Learning*, Vol. 5, 1990, pp. 197–227. https://doi.org/10.1007/BF00116037.

[56] Breiman, L., "Bagging Predictors," *Machine Learning*, Vol. 24, 1996, pp. 123–140. https://doi.org/10.1007/BF00058655.

[57] Thurman, C. S., "The ANOPP2 Artificial Neural Network Tool (AANNT) Reference Manual," NASA TM 20220014856, 2022.

[58] Hendrycks, D., and Gimpel, K., "Gaussian Error Linear Units (GELUs)," *arXiv*, Vol. 1606, No. 08415, 2016. https://doi.org/10.48550/arXiv.1606.08415.

[59] Ramachandran, P., Zoph, B., and Le, Q. V., "Searching for Activation Functions," *arXiv*, Vol. 1710, No. 05941, 2017. https://doi.org/10.48550/arXiv.1710.05941.

[60] Huber, P. J., "Robust Estimation of a Location Parameter," *The Annals of Mathematical Statistics*, Vol. 35, No. 1, 1964, pp. 73–101. https://doi.org/10.1214/aoms/1177703732.

[61] Kingma, D. P., and Lei Ba, J., "Adam: A Method for Stochastic Optimization," *3rd International Conference on Learning Representations, San Diego, CA*, May 2015.

[62] Sobol', I. M., "Global Sensitivity Indices for Nonlinear Mathematical Models and their Monte Carlo Estimates," *Mathematics and Computers in Simulation, The Second IMACS Seminar on Monte Carlo Methods*, Vol. 55, No. 1–3, 2001, pp. 271–280. https://doi.org/10.1016/S0378-4754(00)00270-6.

[63] Cukier, R. I., Fortuin, C. M., Shuler, K. E., Petschek, A. G., and Schaibly, J. H., "Study of the Sensitivity of Coupled Reaction Systems to Uncertainties in Rate Coefficients. I Theory," *The Journal of Chemical Physics*, Vol. 59, 1973, pp. 3873–3878. https://doi.org/10.1063/1.1680571.

[64] Saltelli, A., Tarantola, S., and Chan, K. P.-S., "A Quantitative Model-independent Method for Global Sensitivity Analysis of Model Output," *Technometrics*, Vol. 41, No. 1, 1999, pp. 39–56. https://doi.org/10.1080/00401706.1999.10485594.

[65] Saltelli, A., "Making Best use of Model Evaluations to Compute Sensitivity Indices," *Computer Physics Communications*, Vol. 145, No. 2, 2002, pp. 280–297. https://doi.org/10.1016/S0010-4655(02)00280-1.

[66] Zhang, T., Geyer, T., de Silva, C., and Fischer, J., "Experimental Investigation of Tip Vortex Formation Noise Produced by Wall-Mounted Finite Airfoils," *Journal of Aerospace Engineering*, Vol. 34, No. 6–04021079, 2021. https://doi.org/10.1061/(ASCE)AS.1943-5525.0001315.

[67] Ramasamy, M., Johnson, B., and Leishman, J. G., "Turbulent Tip Vortex Measurements Using Dual-Plane Stereoscopic Particle Image Velocimetry," *AIAA Journal*, Vol. 47, No. 8, 2009, pp. 1826–1840. https://doi.org/10.2514/1.39202.